PHOTONIC CRYSTAL ENHANCEMENT AND TUNING OF QUANTUM DOT EMISSION

BY

GLORIA G. SEE

DISSERTATION

Submitted in partial fulfillment of the requirements
for the degree of Doctor of Philosophy in Electrical and Computer Engineering
in the Graduate College of the
University of Illinois at Urbana-Champaign, 2016

Urbana, Illinois

Doctoral Committee:

Professor Brian T. Cunningham, Chair
Professor Andrew Alleyne
Associate Professor Lynford Goddard
Assistant Professor Songbin Gong

ABSTRACT

The work presented in this dissertation demonstrates various methods and approaches for photonic crystals (PCs) to enhance the output emission and performance of quantum dots (QDs). We integrate visible wavelength emitting QDs within a polymer-based photonic crystal and excite them using an ultraviolet-emitting LED. The PC design incorporates two interleaved regions, each with distinct periods in orthogonal directions to enable simultaneous resonant coupling of ultraviolet excitation photons to the QDs and visible QD emission at two different wavelengths to efficiently extract photons normal to the PC surface. The combined excitation and extraction enhancements result in a 5.8X increase in the QD output intensity. Further, we demonstrate multiple QD-doped PCs combined on a single surface to optimally couple with distinct populations of QDs, offering a means for blending color output and directionality of multiple wavelengths.

Another replica molded PC is fabricated with embedded QDs in which electrohydrodynamic jet printing is used to control the position of the quantum dots within the device structure. This results in significantly less waste of the QD material and the targeted placement of the quantum dots minimizes any emission outside of the resonant enhancement field, enabling an 8X output enhancement and highly polarized emission from the PC structure.

We demonstrate a method for combining sputtered TiO_2 deposition with liquid phase dip-coating of a QD layer that enables precise depth placement of QD emitters within a high-index dielectric film, using a PC slab resonator to demonstrate enhanced emission from the QDs when they are located at a specific depth within the film. The depth of the QDs within the PC is found to modulate the resonant wavelength of the PC as well as the emission enhancement efficiency, as the semiconducting material embedded

within the dielectric changes its spatial overlap with the resonant mode.

The first real-time tuning of PC-enhanced QD emission is successfully performed by fabricating QD embedded PCs on the surface of an acoustic MEMs resonator. As the RF modulation deforms the piezoelectric material of the resonator, the surface PC is also deformed. The coupling wavelength of the PC is modulated away from the QD emission wavelength, producing measurable variation in the output intensity of the QD emission. By tailoring the design and fabrication of QD-embedded PCs, significant improvements in device efficiency and production costs can be realized for utilizing QDs in lighting and display applications.

In memory of the Beckman cuttlefish

ACKNOWLEDGMENTS

I've never been one for the long "I'd like to thank the academy" type speeches, but I'm overwhelmed with how many people helped me along the way to my PhD.

When choosing a grad program, one of my mentors was heavily in favor of the University of Illinois, which he described by saying "When you multiply smart time nice, these guys win." Professor Brian Cunningham was the embodiment of this observation and I'm so grateful for all his advice and support through the challenges of graduate school.

Professor Songbin Gong also spent a tremendous amount of time and effort helping me during the final year of my research and I'd like to thank him and his students for all their knowledge and patience.

To the cleanroom staff, MNTL business office, and ECE Shop staff: We'd never get anything done without you. We would be like those baby birds raised by sock puppets that have no idea how to hunt in the wild or cross the street unsupervised.

My fellow students and collaborators Lu Xu and Anming Gao are doing amazing research. I'm proud to have had the opportunity to work with you, and wish you all the best in everything you do.

During the hardest moments of grad school, Kenny Long and Yemaya Bordain went so far beyond the duties of friends that I spent weeks trying to find the words to describe what our time together meant to me and have yet to find anything close to adequate. I would never have made it without you.

Finally, if there's a single person who is responsible for me staying in engineering as a undergrad, getting my doctorate, and finally having a great Bond-villain-esque title, it is Dr. Jeffrey Clarkson. Thank you for the perfect balance of honesty and optimism.

TABLE OF CONTENTS

LIST OF ABBREVIATIONS

BAW	Bulk acoustic wave
FBAR	Film bulk acoustic resonator
FWHM	Full width, half maximum
LCD	Liguid crystal display
LED	Light emitting diode
MEMS	Microelectromechanical systems
OLED	Organic light emitting device
PC	Photonic crystal
QD	Quantum dot
RF	Radio frequency
SAW	Surface acoustic wave
TE	Transverse electric
TM	Transverse magnetic

LIST OF SYMBOLS AND CONSTANTS

Λ	grating period
ε	permittivity
ε_0	permittivity of vacuum
λ	wavelength
ν	phase velocity
ρ	density
θ	angle of incidence
θ_n	diffraction angle
d_{ij}	piezoelectric coefficient
k_t^2	electromechanical coupling coefficient
m	diffraction order
n	refractive index

CHAPTER 1

INTRODUCTION

Lighting is one of the largest consumers of energy in today's world. The need to improve the efficiency of our lighting materials has driven tremendous research efforts, but the available solutions have yet to overcome the marketplace barriers of cost, ease of use, and consumer appeal. In the case of display technologies, pure color control, high saturation and low power are critical drivers, as displays are high cost elements and major power consumers, especially in mobile applications. By utilizing the spectral and material advantages of quantum dots, combined with the enhancement and directional control enabled by photonic crystal structures, it is possible to create hybrid technologies to help overcome the cost and efficiency issues that are currently obstructing the performance of lighting and display applications.

1.1 Motivation

After heating and cooling, lighting consumes more energy than any other household function. It is also a significant energy drain in business and industrial settings [1]. This makes the improvement of lighting efficiency for residential and commercial use a key growth area, and solid state lighting has attracted interest as a means to improve the efficiency of lighting technology, thus decreasing energy consumption [2].

A variety of government reports have investigated the options for replacing existing incandescent and fluorescent lights with solid state lighting. As of 2011, there were a number of solid state lighting options available to replace fluorescent workplace lighting with lower power consuming options, but the newer lights had as much as 25% lower illuminance and life cycle costs of $100-$700 more per device than the

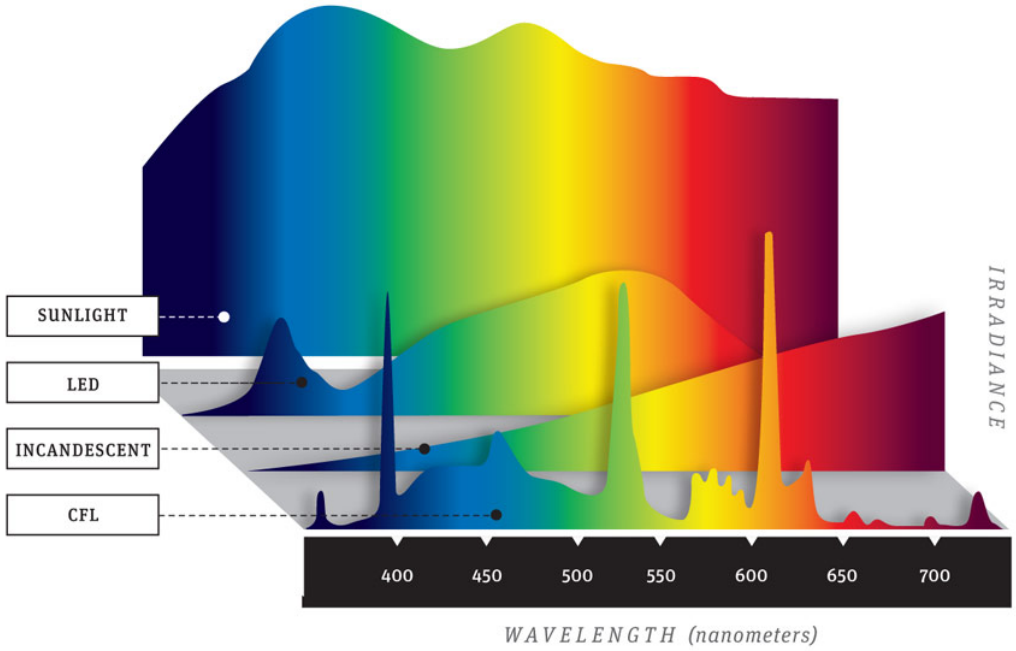

Figure 1.1: The spectral components of several common light sources [4].

incumbent technology [3].

In addition, as shown in Figure 1.1, the spectral composition of solid state lighting tends to be "cooler." Like fluorescent lights, LED light contains a significant contribution from blue wavelengths and has a much lower intensity of yellow and red wavelengths than consumers are accustomed to in sunlight and incandescent bulbs. This aesthetic factor has also slowed the acceptance and usage of LED lighting.

Research to address these shortcomings has produced a range of colors in LEDs and organic light emitting diodes (OLEDs), using a variety of emitters [5]. The transparency of certain devices also allows them to be stacked for full color displays [6]. White OLEDs have also been developed to fill the growing need for backlighting in displays, as well as general lighting applications [2].

OLEDs are becoming cheaper to produce than LEDs and are polymer compatible, making flexible device architectures more easily realized [7]. OLEDs began to reach performance metrics viable for lightweight flat panel displays in the late 1990s [6] and are appearing in some Samsung mobile devices and other consumer applications [8].

However, despite the significant potential for these devices, there are

severe limitations on their manufacturing and performance. Because of issues with heating and lattice mismatch, device areas for most LEDs are limited to 1-2 mm^2 [7]. Research and development on OLEDs has been slower than anticipated, making projections for wide-scale commercial integration difficult [9]. Issues have included serious challenges with emitter lifetimes, color bleeding from blue to red [6], and even molecular orientation in the OLED layers, which has been shown to impact the device performance [10].

A variety of quantum dot integrated LEDs are beginning to approach performances comparable to industry standards and are expected to eventually surpass OLEDs; however, blue and green QD-LEDs are particularly prone to efficiency issues [7], which is a major challenge given the sensitivity of the human eye to green wavelengths [11]. New QD chemistries and novel device architectures are being investigated to push forward the QD-LED performance [12].

By 2030, it is expected that solid state lighting will have grown to 74% of "lumen-hour" sales, representing a cumulative savings of 2700 terawatt hours, $250 billion and 1.8 billion metric tons of carbon emissions [9]. Combined with the potential markets in display applications, there has been interest in bringing improved lighting and display technologies from major industry players, including Samsung, LG, Sony, Panasonic, and Amazon [7, 13].

1.2 Background

1.2.1 Photonic Crystals

Photonic crystals (PCs) are structures that have a sub-wavelength sized periodic variation in their refractive index in one, two, or three dimensions, but are uniform in the non-periodic directions [14]. By modifying the contrast in the refractive index of materials and the feature sizes of the structure, it is possible to design a PC to have specific electromagnetic modes propagate in the structure and to create a photonic bandgap in which no modes can exist for a certain frequency range.

The periodic structure results in variations in the distribution of light,

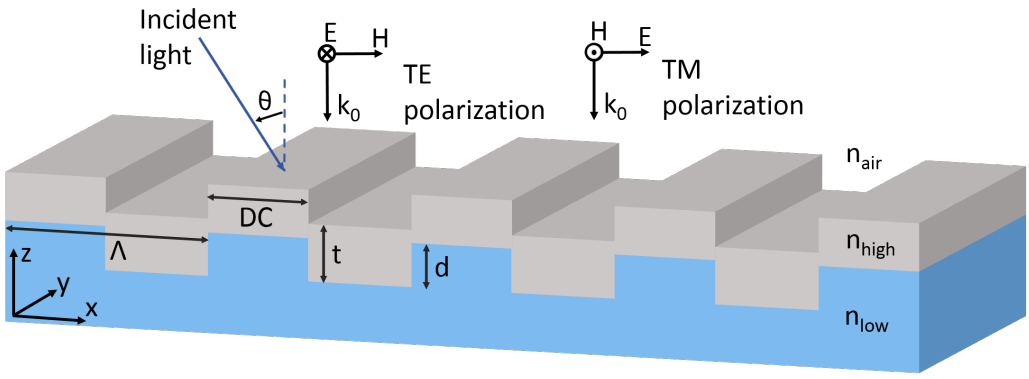

Figure 1.2: The structure of a one-dimensional photonic crystal grating.

depending on its wavelength and incident angle. These variations, first reported by Wood from an incandescent light viewed on a grating [15], consist of a rapid change in the intensity of the diffraction spectra over narrow frequency bands [16]. Because the variation was inconsistent with existing grating theory, it was termed an anomaly, and has since been broken down into two types: Rayleigh and resonance [16].

Rayleigh anomalies can be determined from the grating equation:

$$\sin\theta_m = \sin\theta + \frac{m\lambda}{\Lambda}, \tag{1.1}$$

where θ_m is the diffraction angle, as determined by the angle of incidence θ, the diffraction order m, the free space wavelength λ, and the grating period Λ.

Resonance anomalies occur when the phase matching condition, described by Equation 1.2, is met.

$$k_0 \sin\theta \pm m\frac{2\pi}{\Lambda} = \frac{2\pi}{\lambda} n_{eff} \tag{1.2}$$

with the free space wave number k_0 and the effective refractive index n_{eff} [16–21].

The high refractive index layer of the grating structure, shown in Figure 1.2, can support guided modes. These modes couple light into or out of the PC grating from external illumination sources, leading to guided mode resonance, while the uncoupled light will transmit through the PC as if it is transparent [21–23].

The grating structure also diffracts light into higher orders, which can

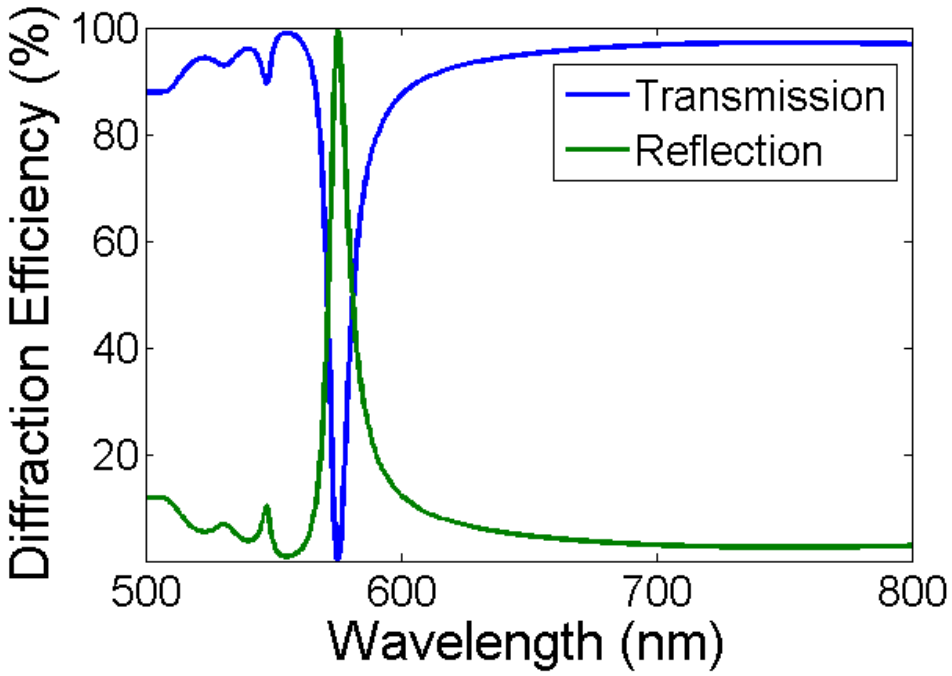

Figure 1.3: The modeled transmission and reflection spectra for a 1D PC grating structure.

interfere with the zeroth order modes. Under phase matching conditions, the light diffracting backwards is in phase with the zeroth order of reflected light, while the forward propagating diffraction destructively interferes with the zeroth order transmitted light [21]. This effectively prevents any light from transmitting through the structure at the phase matching conditions of wavelength λ and incident coupling angle θ, and provides complete reflection, as shown in the example transmission spectrum of a modeled PC in Figure 1.3. This "dip" in the transmitted spectrum through the PC broadens with the resonance conditions and assumes a Lorentzian shape [24].

When an initial field profile is "nearly" guided, it becomes possible for a leaky mode to exist [25]. This occurs as the coupling wavelength at normal incidence will also couple to the $m = \pm 1$ diffraction orders. Because these orders have propagation constants with opposite signs in the PC, they create a resonant optical standing wave, leading to significantly increased electric field intensities within the structure as compared to that of the incident light.

For 3D structures, the existence of a photonic bandgap depends on the

lattice structure of the material. The diamond lattice structure is particularly conducive to photonic bandgaps [26]. Face-centered-cubic is a common lattice structure, but does not have a true gap [26, 27]. In addition, light that is emitted or generated within the in-plane photonic bandgap area can only couple to the radiation modes of the PC, regardless of the dimensions [28], which is a crucial parameter when designing for emitters that are embedded within the PC structure.

The PC structure is also sensitive to the polarization of the incident light. The orthogonal transverse electric (TE) and transverse magnetic (TM) modes can both be supported in a one-dimensional PC, as shown in Figure 1.2, but with different resonance conditions. The TE polarization has an electric field incident along the grating structure of the 1D PC, while in the orthogonal TM mode, the electric field is perpendicular to the grating. TE and TM polarized light will only couple to the corresponding mode types supported within the PC. The TM mode will have a narrower resonance band and occur at a shorter wavelength than the TE mode of the same order. The TE mode has larger diffraction loss and a lower quality factor than the TM mode, and thus the TM modes have a higher field intensity at the surface of the PC [24, 29].

1.2.2 Applications of Photonic Crystals

The simplest photonic crystal consists of a multilayer stack of alternating high and low dielectric materials [30], but even this basic dielectric grating structure of PCs is key for the functioning of Bragg film stacks, dielectric waveguide gratings, and optical reflectance filters. One-dimensional PC gratings have been used to provide enhanced fluorescence [29] for sensors, lasers and filters, active waveguiding [31], and improved waveguiding in PC optical fibers [32].

The first 3D PC was realized by Yablonovitch by drilling a face-centered-cubic lattice of air holes into cubes of Al_2O_3 [33]. Since then, 2D and 3D PCs have also been used for a variety of applications. These range from on-chip control of beam steering of a PC laser in two dimensions [34] and 3D control of light from a 2D substrate [35], to increasing the selectivity and absorption of infrared photodetectors [36, 37]

and guidance in optical fibers [38]. Opal structures have demonstrated strong diffraction [39], and 3D "woodpile" photonic crystals have demonstrated a large (4.5 μm) stop band in the infrared [40], a valuable wavelength range for optical communications.

PCs are also appealing for their ability to enhance the emission or extraction of light from many types of emitters. These range from phosphor films [41] to novel quantum dot (QD) embedded structures, such as a 2D circular dielectric grating in which embedded QD emission was enhanced by a factor of 20X when measured under a flow of liquid helium [42].

The use of PCs to improve the performance of light emitting diodes has also been heavily researched [43]. There has been a continuous progression of improved enhancement factors for the LED efficiency from 25% [44] to 50% [45], up to 3X [46] and 6X [47]. These improvements are due to improved out-coupling of light from the LED device layers by the PC structure and have been demonstrated across a range of active materials within the LEDs and a broad spectrum of output wavelengths [48–54]. The PC also provides directional control of the LED light emission [55]; however, in some cases, random texturing provides a higher extraction coefficient than a PC solution [56], due to the high directionality induced by the PC layer.

A similar thrust has emerged to improve the performance of light extraction from OLED devices by using ordered nanostructures, such as gratings or pyramidal arrays combined with TiO_2 [57] and silica [58] particles, or by incorporating PCs and other nanostructures into the device layers [59–63].

1.2.3 Quantum Dots

Quantum dots (QDs) are nanocrystals of semiconductor material. As the nanocrystal size decreases below the 10 nm threshold, many intrinsic behaviors are altered and become size dependent. This size dependence makes it possible to tune the bandgap and emission, and thus obtain a broad range of properties from different sized particles of the same material [64]. Inside the confined volume of a QD, an electron and hole can recombine, allowing a photon to be emitted. The photon energy is

equivalent to the gap between the highest occupied and lowest unoccupied states in the QD [65]. The quantum size effect in such small particles causes the electronic excitation energy level to increase, and fewer transitions become possible.

The higher percentage of atoms on the surface of a nanocrystal, as compared to bulk materials, also impacts the free energy and other properties of QDs [64]. Surface atoms impact nearly all properties of QDs, including the surface chemistry and solubility of incorporating QDs into polymers or other structures, and in less obvious ways, such as the light emission [64]. The surface also contains many locations and defects where non-radiative recombination can occur. This reduces the luminescent emission of the quantum dots, and generally requires some combination of passivation, larger quantum dots or shell coating to increase the quantum yield [66, 67].

One method to improve the quantum yield is capping the QDs with various ligands, although this has significant effects on the performance of the QDs, their incorporation into other solutions, and the performance within device layers [64]. Another solution is the design and fabrication of core-shell QD structures. There are many possible variations of this design, ranging from abrupt to graded core-shell structures, alloyed cores, and multiple or intermediate shells. Each structure includes trade-offs in terms of quantum yield, quenching, blinking, confinement of charge carriers, long term stability, and interface stress between the layers [68]. Creating high quality QDs that are defect free with both uniform size and shape requires intensive process development [67].

QDs, particularly with a core-shell structure, enable very precise design of emission color and a high quality color-rendering index [68], making them a desirable component of solid-state lighting. These qualities are even more appealing for display applications, where a narrow spectral width provides more saturated primary colors and can cover a larger portion of color gamuts, which are often used to quantify color performance for TVs [65, 68]. A full-width, half-maximum (FWHM) of less than $\lambda = 40$ nm is considered desirable to create appropriately tuned outputs [67], and with QDs, a narrow band luminescence of 15-20 nm bandwidth is possible [64]. Existing phosphors cannot match the high color purity and chromaticity enabled by QDs of this quality [65].

Devices that utilize LEDs as an excitation source, and QDs as optical down-converters to create mixed wavelength outputs, have attracted a significant amount of research and development attention [69], and prototype QD backlights for LCD systems have been successfully demonstrated [70]. In display applications, the optimum emission wavelengths are in the ranges of λ=445-455 nm for blue, 525-535 nm for green, and 620-630 nm for red, in order to achieve the most saturated color gamut [67]. Cadmium selenide (CdSe) quantum dots are particularly well-suited for display applications given that their emission wavelengths are tunable over the visible spectrum [71].

For lighting applications, phosphors and QDs have been mixed as optical down-converters to successfully produce white light [72], and core/shell QDs in red, green and yellow have been combined with blue LEDs to make white light outputs [73]. These types of devices are beginning to approach the metrics required for commercial and consumer acceptance, such as color rendering index (an indicator of how "true" the colors of an illuminated object are) and luminous efficiency [69]. Quantum dot LEDs (QD-LEDs) of multiple individual colors have also been produced, and there has been a continuous drive to improve their photoluminescent efficiency [74].

Current driven QD-LEDs have also been investigated, in which layers of QD materials are incorporated between the functional charge-carrying layers of the LED structure [67]. These QD-LEDS have low quantum yields due to charging and field driven quenching [75], which has led to inverted device structures for improved performance [76]. These displays still have challenges with color gamut [67] and high temperatures also cause unreliable performance [77].

Despite challenges, QDs have started to appear in commercial applications as down-converters for blue backlights, such as in Sony LCD televisions [71] and devices from Samsung [67], as shown in Figure 1.4.

QD devices have potential to be incorporated onto a variety of substrates [65], making flexible displays a viable future option, and increasing the feasibility of large area devices. However, for commercially viable devices, establishing reliability in processing and optimized device structures are key challenges that must be overcome [67].

Figure 1.4: A QD display image over a thin film transistor backplane with 320x240 pixels [67].

1.3 Photonic Crystal Enhanced Emission

Dyes, fluorescent molecules and QDs can all experience modified luminescence within the PC structure. Emission wavelengths near a photonic stop band will experience inhibited spontaneous emissions, while the high-energy edge of a stop-band will instead amplify the emission [78]. Enhanced or controlled emission has been shown for numerous methods of incorporating luminescent material into PCs [79–81].

The PC structure and location of the emitter also impact the output [81] and short versus long range order will affect the emission patterns and extracted modes for light emission enhanced by PCs [58]. The PC enhancement is strongest in close proximity to the surface of the structure, so emission in the bulk or substrate regions will not interact significantly with the enhanced electric field [29, 82].

The electric field within the PC structure is capable of enhancing both the excitation and emission wavelengths of QDs [83], and coupling the emitted light into the modes of the PC. Enhancements as high as 30X have

been shown for InGaAs QDs at low temperatures (78K) inside PCs fabricated through electron beam lithography and ion-beam etching [28]. Although this approach is not feasible for large scale or commercial applications, it is a promising indicator of the potential improvements that can be achieved with photonic crystal enhancements of QDs.

The key considerations for display technology performance are output intensity, emission direction, polarization, and spectral profile. By combining the high quality spectral output of QDs with the intensity enhancement, angular control and polarization capabilities of PCs, significant performance improvements for lighting and displays, as well as novel device structures and applications, can be achieved.

1.4 Photonic Crystal Control through the Use of MEMS Devices

1.4.1 Tunable Photonic Crystals

Photonic crystals have been integrated into microelectromechanical systems (MEMS) for a variety of applications. These include a MEMS actuated PC optical switch [84], which demonstrated an optical bandwidth of 65 nm, a MEMS scanner with transfer-printed PC mirrors [85], micro-displacement PC waveguides proposed for sensing [86, 87], and reconfigurable PCs for switching, modulation, resonators or delay lines [88].

Because PCs can be utilized in such a wide range of applications, there are significant advantages to a device that is tunable and can have its resonance modified in real time. Many methods accomplish this modification by adjusting the refractive index of materials within the PC. This may be through an applied electric field [89, 90], magnetic field [91, 92], or temperature changes to the PC material [93–95].

There are also a variety of ways to tune a PC by applying mechanical stress or strain. For example, compressing colloidal crystals in a hydrogel matrix to decrease the lattice constant of the PC has produced nearly 200 nm of tuning across the visible spectrum [96]. A similar structure of silicon rods embedded in low index SU-8 was mechanically stressed by

electro-thermal actuators to provide variation in the period of the PC, and thus its photonic bandgap [97]. A variety of mechanical strain designs for tuning PCs have been extensively studied through simulation [98–102], and show significant theoretical promise.

Another tuning approach utilizes coupled cavity PCs. Numerous modeling and simulation efforts have demonstrated that varying either the distance between two vertically "stacked" PC slabs [103] or the width of a gap that can be treated as a line defect within a PC slab [104] will theoretically allow changes in the Q factor as well as the transmission and reflection coefficients of the PC.

In general, coupled cavity approaches for PC tuning depend on integrating PCs into microelectromechanical systems (MEMS) to provide mechanical displacement. A variety of zipper cavities, in which nanobeams of single ladders of PCs are actuated mechanically, piezoelectrically, or with electrostatic forces applied directly to the beams, have been used as laser cavities [105]. PC resonances have been modulated by $\Delta\lambda = 9.5$ nm of resonance shift [106], and approaching $\Delta\lambda = 19$ nm [107]. Another device architecture of nanocavities on a MEMS comb drive with a varied cavity gap demonstrated an 8 nm resonance shift [108].

An additional method of PC tuning is to fabricate the device using a piezoelectric material as one of the periodic layers of the PC. This is a particularly appealing approach for PCs designed to produce emission enhancement, as it limits external factors that might impact the behavior of the QDs or other emitters.

There have been attempts to demonstrate piezoelectric control of PC devices. Strain tuning applied to quantum dots coupled to a photonic crystal cavity successfully red-shifted the quantum dots; however, the maximum shift was only 0.45 nm with an applied voltage of 15 kV/cm [109]. A one-dimensional photonic crystal mounted on a membrane with piezoelectric actuators demonstrated a resonance shift of 1.54 nm shift under piezoelectric-induced strain [110].

Bormashenko et al. demonstrated a PC of self-assembled polycarbonate on a piezoelectric substrate of polyvinylidene fluoride. The structures demonstrated a photonic bandgap in the infrared, with the potential to be mechanically or electrically tuned [111], although no further work from that group successfully demonstrated tuning in the PC.

A complete phononic bandgap to stop the propagation of acoustic waves across a bandwidth of approximately 25 MHz in a piezoelectric crystalline structure has previously been demonstrated [112]. A phononic crystal into the GHz range on lithium niobate piezoelectrics has also been analyzed for acoustic bandgaps in the GHz range [113].

In the optical regime, a photonic crystal consisting of a hexagonal array of holes in an air/silicon matrix over a piezoelectric substrate has been theoretically proposed for the infrared wavelengths used for optical communications. The piezoelectric deformation with 3% applied shear strain has been calculated to red-shift the bandgap and exclude nearly 75% of the original bandgap [114]. Another structure has been proposed which uses a surface acoustic wave to adjust the refractive index n of layers within a 1D Bragg stack to frequency shift the reflection and transmission bands of the device [115].

1.4.2 Piezoelectric Materials

The defining characteristic of piezoelectric materials is that they experience an induced polarization when stress is applied. An external bias voltage causes deformation in the material, and, likewise, applied pressure that deforms the material causes an induced voltage.

For a piezoelectric effect to be present, there must be an asymmetry in the lattice structure of the material. This allows applied stress to change the distance between electric dipoles, which results in a decrease in the electric field (and thus voltage) as those charges are separated. For the piezoelectric effect to occur in a bulk material, rather than minute amorphous regions, a technique called poling is used. During poling, the material is heated and an external electric field is applied until the material has cooled.

The piezoelectric coupling of a material is described by an 18-element "d-matrix" of strain constants which relate the mechanical displacement to the applied electric field on the material. Each element in the matrix describes a different directionality of the coupling, as they may not always occur in the same direction. When charge is collected along a set surface, the key coefficients are d_{33}, for which force is applied along the polarization

Table 1.1: Key properties of common piezoelectrics materials.

	AlN	LN	PZT	ZnO	PVDF
d_{31} $\left[\frac{pC}{N}\right]$	-1.9 [117]	-1.0 [118]	-171[1] [119]	-4.7 [119]	-23 [119]
d_{33} $\left[\frac{pC}{N}\right]$	-3.4 [120]	6-16 [118]	80-593[1] [119]	12 [119]	-35 [119]
ν_L $[10^3 \frac{m}{s}]$	10.4 [116]	0.35 [121]	4-6 [116]	6.35 [116]	
ε_r	9.5 [116]	28.1-85.2[2] [118]	80-400[2] [116]	9.2 [116]	8.4 [122]
k_t^2 [%]	6.5 [116]		8-15 [116]	7.5 [116]	

[1] Value is for PZT-5.

[2] Value is directionally dependent.

direction on the same surface as charge collection, and d_{31}, where force is applied orthogonal to the polarization, but charge collection is unchanged.

The key material properties of piezoelectric materials vary by application. Large coupling coefficients are often desirable, but not all elements may be comparably useful in the final device. For the particular case of piezoelectric resonators (described in Section 1.4.3), the coupling coefficient k_t^2 indicates the possible exchange between the electrical and mechanical energy domains.

The longitudinal velocity ν_L of a material impacts the device size and piezoelectric layer thickness [116]. The impedance of a resonator is affected by its size and the thickness of the piezoelectric layer, as well as the dielectric constant ε_r of the material, where a larger ε_r allows for a smaller resonator size and impacts the acoustic performance of a resonator's operating frequency [116]. The material properties of some popular piezoelectrics are summarized in Table 1.1.

Aluminum nitride (AlN) is a popular piezoelectric because of its material properties and the fact that, unlike zinc oxide (ZnO) and lead zirconate titanate (PZT), it is CMOS compatible [123] and it maintains its piezoelectric properties in temperatures up to 1200°C [124]. Although it does not have the highest piezoelectric coefficients of available materials, there is a significant advantage in the ease of processing AlN over a

polymer or lithium niobate.

1.4.3 Acoustic Wave Resonators

Microelectromechanical systems (MEMS) resonators take a variety of forms, depending on their application. When used for radio frequency (RF) filtering and channelization, there are several acoustic wave resonator device structures that are commonly used [121]. Surface acoustic wave (SAW) and bulk acoustic wave (BAW) resonators are predominant.

Acoustic wave resonators depend on the relatively slow velocity of sound through solids, as compared to the velocity of an electromagnetic wave. The piezoelectric effect is used to couple energy between the acoustic and electrical domains. The resonator is excited when an electric field is applied to electrodes (usually planar or interdigitated), causing the device to vibrate along specific modes [116, 124]. Similar to photonic modes appearing in a PC as the grating dimension approaches optical wavelengths, acoustic modes appear in an acoustic resonator as the size of the device approaches acoustic wavelengths [116].

In BAW resonators, also known as film bulk acoustic resonators (FBAR), the resonance occurs as a vertical standing wave in the layer of piezoelectric material sandwiched between two electrodes, as shown in Figure 1.5. The thickness of each of these layers determines the resonance frequency of the device [116].

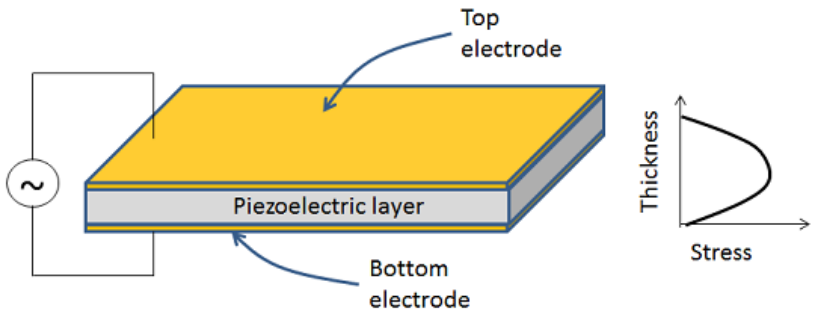

Figure 1.5: Schematic diagram of a BAW resonator, where the piezoelectric material is sandwiched between two metal electrodes [125].

In SAW resonators, the acoustic wave is induced by interdigitated electrodes that transduce the driving electrical signal into the acoustic

mode, which travels along the surface of the resonator. Another set of electrodes transduce the acoustic wave into an electrical output signal. A schematic of this type of resonator is shown in Figure 1.6.

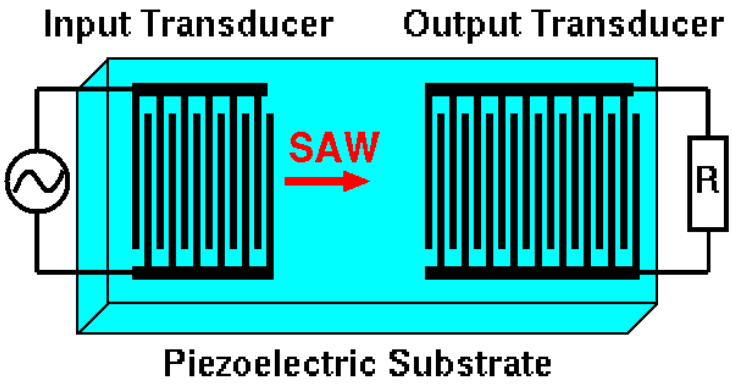

Figure 1.6: A diagram of a SAW device with interdigitated transducers for converting the acoustic surface waves to and from electrical signals [126].

The center frequency f_0 of a SAW resonator is determined largely by the dimensions of the excitation electrodes, as shown in Equation 1.3, where ν is the acoustic velocity of the material, and W_p is the pitch of the interdigitated electrodes [121]:

$$f_0 = \frac{\nu}{2W_p}. \tag{1.3}$$

The electromechanical coupling coefficient k_t^2 is determined by the piezoelectric parameters of the resonator material combined with the design of the electrodes [121].

The optimal design of any acoustic wave resonator is affected by a variety of design parameters including the resonator geometry, topology, signal voltage, and material properties [127]. The size and location of the anchors that support the resonator are also known to impact energy loss into the surrounding environment and decrease the quality factor Q of the resonator [121].

Acoustic wave resonators can be fabricated with standard MEMS processing. This is advantageous because of the compatibility with existing cleanroom fabrication processes, enabling bulk MEMS production across a single wafer [124].

1.4.4 Piezoelectric Control of a Photonic Crystal

As described in Section 1.4.1, the use of piezoelectric displacement to tune a photonic crystal has been demonstrated; however, adequate driving voltage is required to create a useful shift in the resonance condition of the PC. For the case of the linear PC gratings demonstrated in Chapter 3, at least 10 nm of grating deformation is required to produce a resonance shift capable of modifying the emission of the embedded QD layer by $\Delta\lambda \approx 15$ nm. For an AlN piezoelectric device, the required driving bias is on the order of 1 kV for a DC signal.

By using an AC driving signal to induce piezoelectric displacement, the deformation of the PC can be 1-2 orders of magnitude larger than that of previously demonstrated devices. By using an electrically controlled RF resonator to tune PC resonance, real-time control of the extraction modes of the PC is possible. This capacity will enable pixel level control of QD emission for display technologies.

In addition to creating control at a pixel level for enhanced QD emission, electrically tunable PCs have potential applications in communications and data storage if appropriate switching speeds and bandgap controls can be demonstrated [114].

CHAPTER 2

REGION SPECIFIC ENHANCEMENT OF QUANTUM DOT EMISSION USING INTERLEAVED TWO-DIMENSIONAL PHOTONIC CRYSTALS

The power efficiency, spectral characteristics, and output directionality of light emitting diodes (LEDs) used for lighting and video display may be tailored by integrating nanostructures that interact with photon emitters. In this work, we demonstrate an approach in which visible-wavelength-emitting quantum dots (QDs) are integrated within a polymer-based photonic crystal (PC) and excited by an ultraviolet-emitting LED. The PC design incorporates two interleaved regions, each with distinct periods in orthogonal directions. The structure enables simultaneous resonant coupling of ultraviolet excitation photons to the QDs and visible QD emission at two different wavelengths to efficiently extract photons normal to the PC surface. The combined excitation and extraction enhancements result in a 5.8X increase in the QD output intensity. Further, we demonstrate multiple QD-doped PCs combined on a single surface to optimally couple with distinct populations of QDs, offering a means for blending color output and directionality of multiple wavelengths. Devices are fabricated upon flexible plastic surfaces by a manufacturable replica molding approach.

2.1 Introduction

There are a broad range of application-specific needs for lighting and display technologies, given their prevalence in our homes, workplaces and pockets. Precisely engineered control of the output spectrum of lighting products is desired to match the requirements for color temperature and

Material in this chapter is reprinted with permission from G. See et al., "Region specific enhancement of quantum dot emission using interleaved two-dimensional photonic crystals," *Applied Optics*, vol. 15, iss 9, pp. 2302-2308, March 13, 2105.

output directionality, while at the same time optimizing power efficiency and manufacturing cost. For video display applications, controlling the blend of primary colors in each pixel is necessary, while the control of pixel output directionality must be tailored for a range of viewing methods that may be either tightly confined (for privacy) or widely dispersed (for wide viewing angle).

As the effects of polarization, wavelength and directionality within periodic dielectric structures are characterized [14, 16, 128, 129], various applications continue to emerge for optical resonators using photonic crystal (PC) structures. By varying the duty cycle, period, and refractive index, the resonant characteristics of a PC can be tuned to interact with wavelengths extending from the ultraviolet [130] to the infrared [131, 132]. These properties have been used for a variety of applications including polarizers, filters [22], biosensors [82], optical communication components [133], displays, and lighting [134]. PCs have been incorporated into light emitting diodes (LEDs) in order to increase extraction efficiency [56], and to control the directionality of light output, either normal to the device or into angular sidelobes [54, 55].

With an appropriate choice of dielectric materials and dimensions, the resonant modes of a PC can be engineered to occur at specific combinations of angle and wavelength. This allows light of the selected wavelength and incident direction to couple to the PC and excite a highly localized electromagnetic standing wave with an amplitude that is substantially greater than the original illumination source. Enhanced excitation will occur by placing emitters within the region with an increased electric field magnitude at their excitation wavelength. Because the guided modes will couple in and out of the PC under phase matching conditions for specific combinations of wavelength and incident angle, it is possible to collect light at the outcoupling angle more efficiently, thus providing an enhanced extraction mechanism.

Quantum dots (QDs), semiconductor nanocrystals that down-convert light from a broad band of excitation wavelengths to a very specific emission wavelength [81, 135], have been successfully incorporated into PCs with specific resonances designed to couple to the relevant excitation and/or emission wavelengths of the QDs [79, 81, 83, 131, 136–138]. By introducing two-dimensional variation into the PC structure, through the

use of different periods in orthogonal directions, a PC may incorporate multiple resonances at widely varied wavelengths [129] so as to interact simultaneously with the excitation and emission spectra of the integrated QD emitters [83] as a means of enhancing the number of photons generated by each QD, while increasing the efficiency of emitted photons that reach the viewer.

In this work, we demonstrate an approach, shown in Figure 2.1(a), which incorporates one or more types of QDs into a replica-molded flexible polymer-based PC structure that is excited by a UV backlight LED. The UV excitation source couples to a resonant mode of the PC, which creates an enhanced excitation at the coupling wavelength by increasing the magnitude of the electric field experienced by the QDs in the PC, thus producing greater photon output than would occur without a PC structure. The rectangular lattice of the PC is designed to produce a resonance at the wavelength of QD emission, resulting in photon emission that is efficiently channeled normal to the PC surface. As shown in Figure 2.1, we designed and fabricated an interleaved surface in a checkerboard pattern, containing two PC designs. While both regions are designed to produce resonances for the same UV excitation wavelength, each region is optimized for a different QD emission wavelength. This is a novel device structure that allows multiple types of QDs to experience simultaneous enhancement in a single device structure. Such a structure can enable a customized output spectrum through control of the enhancement wavelengths and the relative surface area of each PC region.

2.2 Device Structure

The device structure interleaves the regions of two distinct 2D PCs in a checkerboard pattern. Each region consists of rectangular cavities, as shown in Figure 2.1(b), with resonances created by the periodic variation in the orthogonal directions on the surface. Each region varies in one direction with dimensions selected to provide enhancement from the same UV excitation source (200 nm period with 40% and 70% duty cycles in Regions 1 and 2, respectively), while the orthogonal directions have larger feature sizes for producing resonances at visible wavelengths. The larger features in

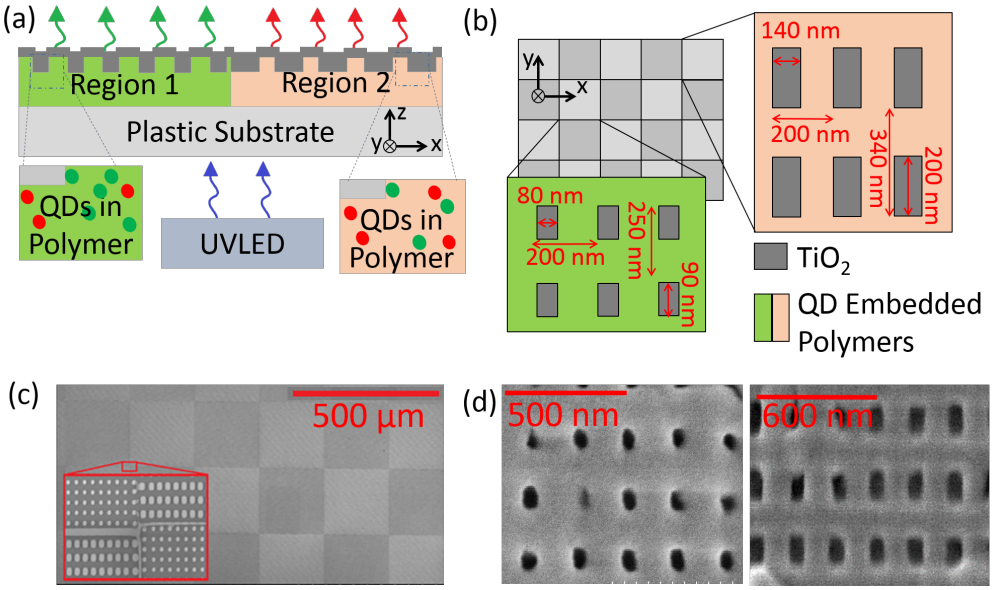

Figure 2.1: The 2D PC device structure: (a) A cross sectional schematic of the device structure in which a backlight UV LED source illuminates multiple regions. Each region contains the same QD mix embedded into the polymer layer of the PC grating. However, the two regions have distinct PC structures to enhance and outcouple separate wavelengths of QD emission. (b) A top-down schematic of the two interleaved regions of the device with TiO_2 and their respective feature sizes. (c) An SEM of the replica molding master. The inset shows the pillars of the two regions at diagonal corners within the master structure. (d) SEM images of both Region 1 (left) and Region 2 (right) from the device after TiO_2 has been deposited to form the PC.

Region 1 have a lateral width of 250 nm to produce resonances at λ=490 nm, while the features in Region 2 have a lateral width of 340 nm, designed to produce resonances at λ=590 nm. For both regions, the structure is formed from a QD-doped polymer with a grating depth of 80 nm that is coated with an 85 nm thin film of TiO_2. While the period of the structure is the main determinant of the resonant wavelength, the resonances can also be tuned via control of the TiO_2 thickness.

The PC structures were designed using rigorous coupled wave analysis (Rsoft, DiffractMod) to predict the resonant wavelengths and electromagnetic field distributions at the resonant wavelengths, by evaluating a unit cell of the PC with periodic boundary conditions in both the x- and y-directions, as indicated in Figure 2.1. Note that, due to the large difference between the refractive index of TiO_2 in the UV (n=2.87) [139] and the visible (n=2.61 at λ=590 nm) [139], separate simulations were carried out for unpolarized incident light in two wavelength bands ($350 < \lambda < 450$ nm, and $450 < \lambda < 800$ nm) and plotted together for each PC region. The simulation results (Figure 2.2) show large dips in the transmission efficiency at the wavelengths for which guided mode resonance occurs. Both regions have resonances in the UV near λ=370 nm, and Region 1 has a resonance near λ=490 nm, while Region 2 has a resonance near λ=600 nm. These visible wavelength resonances are designed to overlap with the emission spectra of QDs incorporated into the PC.

2.3 Materials and Methods

A silicon wafer was fabricated to serve as a master template for the replica molding process, and thus contains a negative surface image of the desired PC grating structure. The master grating structure was fabricated via electron beam lithography on a layer of thermally grown SiO_2 on a Si wafer, upon which reactive ion etching was used to produce 80 nm tall pillars, as shown in Figure 2.1(c). The patterned device area was 3 x 3 mm^2. To facilitate the clean removal of the replica from the master, the wafer was cleaned with a piranha solution (3:1 (v/v) mixture of sulfuric acid and hydrogen peroxide) for 20 min, rinsed with DI water (MilliQ), and dried

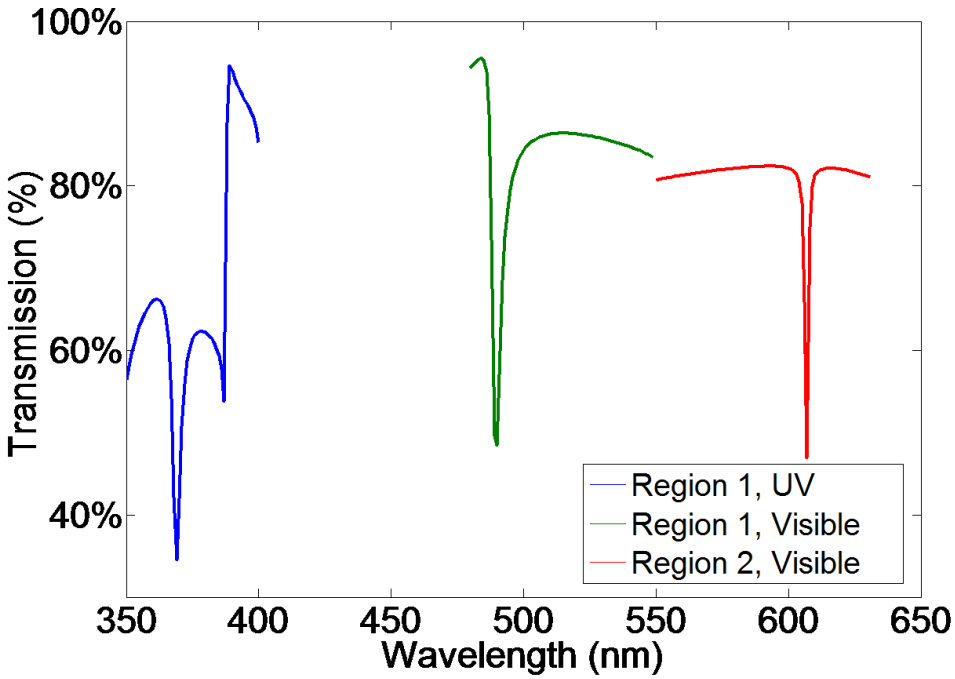

Figure 2.2: Computer-simulated transmission spectra of target resonances occurring with an unpolarized source at normal incidence for Region 1 and 2. Because of the variation in the refractive index values of TiO_2 at different wavelengths, the simulations were run with the appropriate values for each wavelength range.

with N_2. Next, a vapor-phase deposition of (tridecafluoro-1,1,2,2-tetrahydrooctyl) trichlorosilane (No-Stick, Alfa Aesar) was performed by placing the wafer into an enclosed container with two drops of the No-Stick solution for 1 h.

CdSeS/ZnS alloyed QDs were purchased from Sigma-Aldrich (6 nm, 1 mg/mL in toluene, oleic acid as ligand), or synthesized for this application by coating with oleic acid ligand, then purified twice using precipitation and centrifugation with ethanol and methanol. Lauryl methacrylate (LMA) and ethylene glycol dimethacrylate (EGDMA) (Sigma-Aldrich) were purified to remove the inhibitor with an inhibitor-removal column (Sigma-Aldrich) before their use.

The UV curable polymer, consisting of 182 μL of LMA and 18 μL of EGDMA, was mixed in a flask, and 4 mL of the QD hexane solution and 8 μL oleic acid was added and mixed well, then 20 μL of PLMA monopolymer solution (Scientific Polymer Products, Inc.) was added to increase the viscosity. The remaining solvent was removed using a rotavap at room temperature and 2 μL of initiator (Darocur 1173, Sigma-Aldrich) was added immediately before spin coating. The solution was spin coated onto the master wafer at 600 rpm for 30 s, then immediately polymerized by exposure to a high intensity UV lamp for 30 min in an argon atmosphere glovebox.

After the film was fully cured, a layer of NOA 61 (Norland Products Inc.) was drop coated over the composite film. An acetate sheet (Optigrafix Acetate) substrate, selected for low birefringence, was then placed over the master wafer and brought into contact with the uncured NOA drops to form a thin continuous layer between the acetate sheet and the composite thin film. Next, the NOA was cured for 10 min using a UV lamp under ambient conditions. The acetate substrate, along with the NOA layer and composite thin film, was then released from the master wafer with the thin film of QD-PLMA containing the replicated 2D cavity structure. After replica molding, TiO_2 was deposited by sputtering (K. J. Lesker Dual-Gun Sputter System) to the depth required for resonance at the desired wavelength. Deposition times were restricted to keep the substrate temperature from exceeding 40°C, to avoid thermally induced damage to the polymer materials, which sometimes required multiple layers of TiO_2 deposition to reach the correct thickness.

2.4 Results

The emission properties of the devices were measured using a UV LED (Thor Labs, Ultra Bright Deep Violet LED) centered at λ=375 with a 20 nm full-width half-maximum as the excitation source. A 350< λ <390 nm bandpass filter was used to eliminate any non-UV emission from the LED. The LED output was collimated before illuminating the PC. The device was mounted over a cover with a 3 mm diameter aperture, assuring that only the patterned PC region was excited and measured.

The device under test was mounted to a motorized rotary stage, allowing the incident excitation angle to be varied. The output passed through a UV filter to eliminate any light from the excitation source, then was collected by a collimating lens attached to an optical fiber. The fiber was connected to a spectrometer (USB2000+, Ocean Optics) from which the emission can be measured and observed through the LabView OmniDriver software which also controlled the rotation position of the stage in 0.1° steps.

To measure the impact of the extraction angle, the same equipment was used, but instead of mounting the PC sample to a rotation stage and varying the excitation angle, the PC sample position was fixed. The collimator coupled to the optical fiber was instead mounted on the stage and rotated around the PC, allowing extracted light to be collected over a range of angles with respect to the PC surface.

The photonic band diagram of a device was determined using the same experimental setup as that to measure the excitation output, but the UV LED and associated bandpass filter were replaced with a tungsten-halogen lamp coupled to an optical fiber that outputs unpolarized light through a collimator, then the broadband transmission was measured across a range of angles.

In a sample with QDs emitting at a peak wavelength of λ=505 nm, the extraction was measured before and after a deposition of 20 nm of TiO_2 to compare the output intensity with and without a photonic crystal structure, as shown in Figure 2.3. A narrow, angle dependent extraction enhancement is shown, in addition to a broader excitation enhancement. Another sample was fabricated with a homogeneous mixture of QDs, with emissions centered at λ=490 nm and λ=585 nm. This mix demonstrated the ability of the PC to selectively enhance a sub-population of embedded

QDs. The emission was measured on a QD-doped grating structure without PC resonances by measuring the emission of a structure without TiO_2 (Figure 2.4(a)) and after the PC is formed by deposition of a 43 nm TiO_2 thin film. The maximum QD emission increased by 4 times for the 490 nm QDs and 5 times for the 585 nm QDs, shown in Figure 2.4(b), but only within the regions in which their emission matched their corresponding PC resonance. To adjust the resonance conditions of the PC for enhancing the emission wavelengths of both types of QDs, an additional 42 nm of TiO_2 was deposited, and that resulted in a total increase of 4.2X for the 490 nm QDs and 5.8X for the 585 nm QDs (Figure 2.4(c)), as the resonance conditions of the PC were red-shifted by the thicker TiO_2 layer. After the final TiO_2 deposition, the band structure of the PC was measured using the broadband source, as shown in Figure 2.4(d).

Because the device structure has a different period in each orthogonal direction, the transmission efficiency can be measured over the range of angles across θ that vary with the shorter, UV resonant features or the ϕ angle with the larger features that couple to visible wavelengths. The difference in the two photonic bands is shown in Figure 2.5. In Figure 2.5(a), the angle θ is varied; there is an angle-dependent resonance in the UV, while the resonance in the visible is constant for all wavelengths, regardless of angle. This occurs because there is no angle variation experienced by the features responsible for coupling to those wavelengths. A similar situation occurs in Figure 2.5(b) with constant wavelength resonance occurring in the UV wavelengths, while varying the angle ϕ experienced by the PC only changes its coupling to the larger PC features and shows angle dependent variation at wavelengths greater than λ=450nm.

The enhancement of QDs in a region with PC coupling is substantial enough to be easily visible to the naked eye. Figure 2.6 shows photographs of two dual-region QD-doped PCs with emissions at λ=490 and λ=590 nm. The brighter regions are providing both enhanced excitation and extraction for the embedded QDs. The alternate regions have a resonance condition of the PC that is coupling only to the excitation wavelength, and appear darker due to the lack of an extraction enhancement.

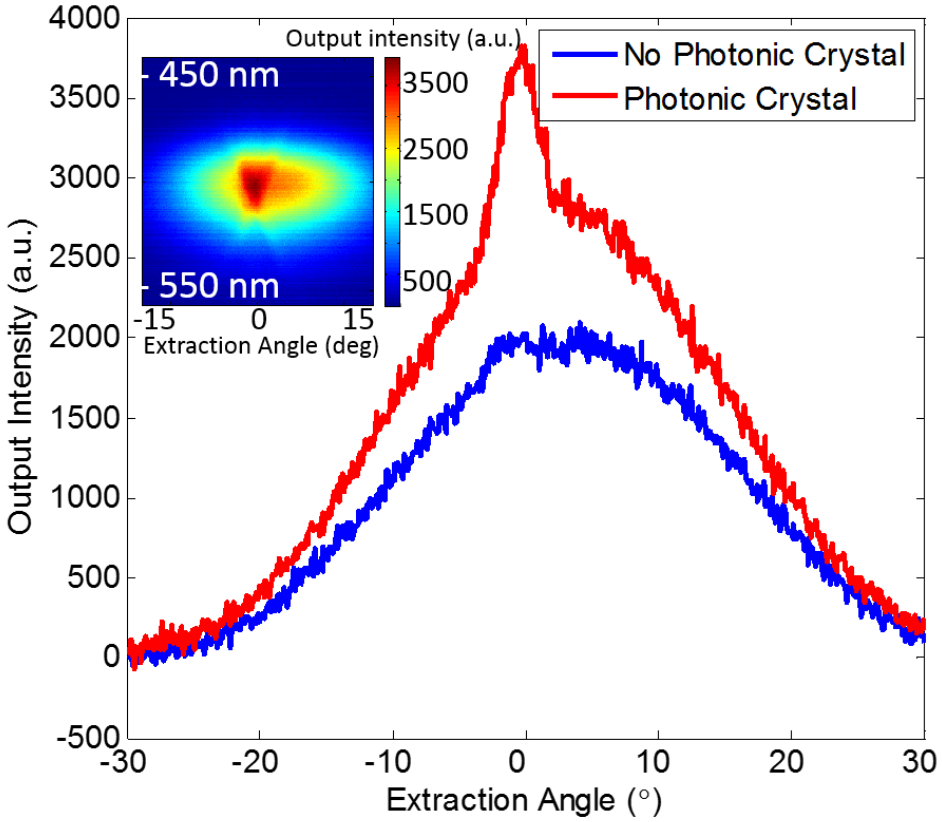

Figure 2.3: The impact of angle on QD extraction measured with and without a PC structure present. In the inset, a scan of the output intensities for λ=450-550 nm across a range of angles is shown in a device with a 20 nm TiO_2 thin film coating. In the main plot, the angle dependence of the output at λ=505 nm is shown. With no PC present, the output emission of the quantum dots is lower. In the structure with the PC, there is a strong angle-dependent enhancement of a factor of 2X centered at -2° off normal incidence, representing the angle and wavelength combination at which the QD emission is enhanced through resonance with the PC.

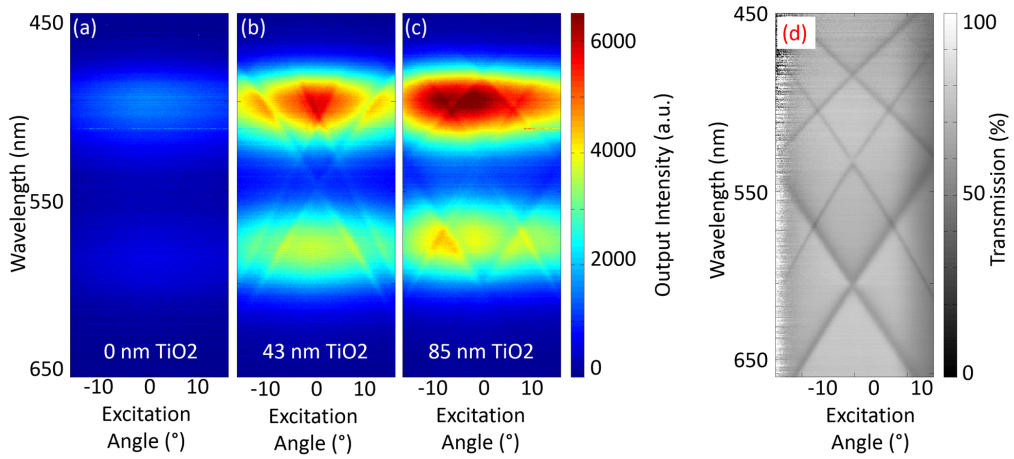

Figure 2.4: A comparison of the angle dependence of excitation at different stages of TiO_2 deposition, as the thickness enables tuning of the resonance conditions: (a) The measured output intensity with no PC structure, (b) measured enhancement from a PC with a 43 nm thick TiO_2 layer, (c) measured enhancement from a PC with an 85 nm think layer of TiO_2, (d) the transmission spectrum with an 85 nm think layer of TiO_2 confirms the locations of the peak resonance as measured by the varied excitation output intensity in (c).

2.5 Discussion

The QD excitation measurements for structures with and without a PC structure all showed a slightly asymmetrical output, which corresponded to asymmetrical output intensity from the UV-LED source. This can be seen in Figure 2.3, where the peak extraction occurs at -2° from normal incidence. This narrow peak is angle dependent, and shows a factor of 2 increase in output emission with the photonic crystal present, while the broader enhancement across all measured angles is due to the enhanced excitation over the entire PC area. The extraction enhancement occurs only in the PC region, but both regions have resonances at the UV excitation wavelength and so contribute to the enhanced excitation. As shown in Figure 2.5, the UV and visible resonances show angle dependence in orthogonal directions, so it is expected that the enhanced excitation shows little angle dependence when varying the extraction angle.

By adjusting the thickness of the TiO_2 layer, the resonance conditions can be easily tuned. As shown in the varied depositions in Figure 2.4(a-c),

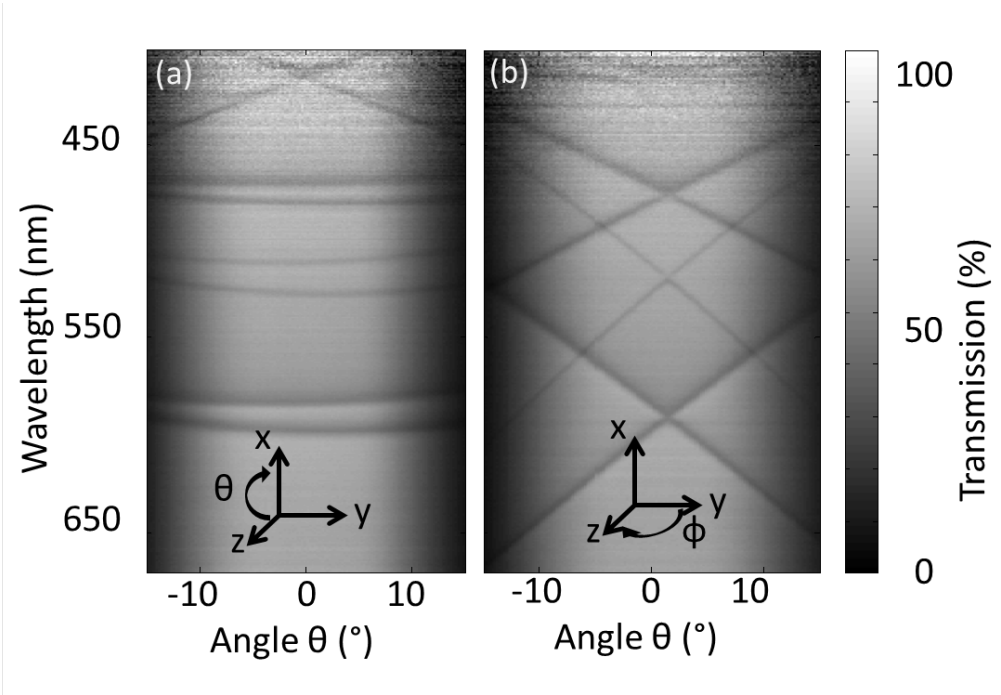

Figure 2.5: The resonance conditions for the UV and visible wavelengths occur in orthogonal directions, so (a) the transmission measured only with angle variation along θ has angle dependence in the coupling to the UV wavelengths. In (b), the ϕ variation leads to angle dependent coupling with the visible wavelengths. The features of the photonic band diagram are less distinct for λ <450 nm because the broadband light source emits visible wavelengths λ >450 nm.

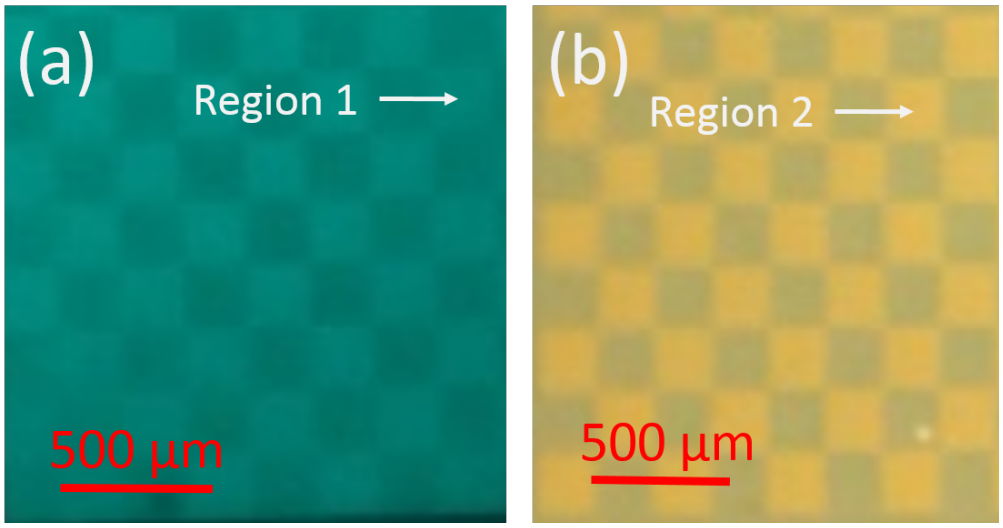

Figure 2.6: Photographs of quantum dot enhancement within the checkerboard of PC regions: (a) The QD emission at λ=490 nm is brighter in Region 1, where both the excitation and extraction are being enhanced, compared to Region 2, in which only enhanced excitation occurs. (b) Sample with a mix of QDs emitting at λ=490 nm and λ=590 nm. The yellow QDs in Region 2 dominate the output because the peak extraction enhancement for λ=490 nm in Region 1 is directed away from normal, resulting in reduced intensity when observed from above the PC.

a thicker layer red-shifts the resonance wavelength of the structure. Figure 2.4(d) shows the photonic band diagram of the structure with the total 85 nm of TiO_2, where the darker bands indicate the wavelength and angle coupling leading to resonance within the PC. These bands correspond to the bands of enhancement seen in Figure 2.4(c) within the QD emission.

Devices using the PC structure demonstrated in this work combine excitation and extraction enhancement for an increase of up to 5.8X as compared to the QD output produced with no PC structure present. There is an expected difference between the improvements in excitation and extraction, given that the QDs are dispersed through both regions of the PC structure. Therefore, the QDs in every region experience enhancement of the UV excitation wavelength, but the output wavelengths are enhanced only in one region, or half the total device area.

There are also several mechanisms by which it will be possible to further improve the enhancements offered by this approach. By optimizing the feature sizes for specific colors, the PCs may be designed to better couple to the emission and excitation wavelengths of the desired QDs, increasing the local electric field within the PC, and thus the enhancement experienced in the QD output. This can also be accomplished by coupling QDs to only the TM mode, with higher Q-factor resonance conditions. In a 1D PC, the TM mode (which has electric field components in the x- and z-directions) can be isolated from the TE mode (with only y-directional electric field). However, in a 2D PC, the two polarizations cannot be separated and present as TE- and TM-like modes. These modes are similar to their 1D counterparts, with the TM-like mode occurring at a longer wavelength and having a narrower resonance than the TE-like mode, as shown in the band diagram in Figure 2.4.

In addition, the lattice structure in the PC has a dramatic effect on the possible enhancement, as shown in [82, 137], where square and hexagonal arrangements of circular cavities demonstrated enhancement factors of 100-200X. Specifically placing the QDs only in the PC pixel region where they would experience both excitation and extraction would decrease the quantities of QDs required and also extract light more effectively. With these improvements, it is likely that the PC enhancement would be at least comparable to the 8X enhancement reported in [83].

Future devices may be designed to utilize a non-UV excitation source

simply by adjusting the design parameters to couple to a different wavelength. Pixel patterning can also create regions with no PC structure at all, allowing only the excitation source light to pass through, thus increasing the flexibility of color mixing options for lighting.

The use of nanoreplica molding for fabrication makes it possible to scale up to large area fabrication on flexible substrates. With appropriate materials, large area, flexible displays and light sources can be constructed to use pixelated PC enhancement. The use of PCs in lighting and displays gives the advantage of angle steering possible with PC enhancement to broaden or narrow the output angles and control the directivity of light output in both lighting and displays. Polarization control is also possible with a PC, and could eliminate the 50% loss of backlight power by providing an initially polarized output in display technology.

The technological opportunities afforded by PCs combined with the levels of enhancement possible using QD-embedded PC devices may be a key enabler for the affordable incorporation of QDs into novel lighting and display applications. The enhancements require lower concentrations of QDs and could advance the color purity and performance of QD-based light sources towards consumer applications.

2.6 Conclusions

The devices in this work demonstrate the incorporation of QDs into a replica molded 2D PC. The PC has distinct periods in orthogonal axes, allowing one direction of the structure to resonantly couple the UV LED excitation source to the embedded QDs. The orthogonal direction resonantly couples to the QD emission in the visible spectrum, enhancing the extraction of photons normal to the device surface. These structures have demonstrated combined excitation and extraction enhancements up to 5.8X output intensity, using an approach that interleaves PC regions and enables design-selectable resonant properties, allowing different types of QDs to be embedded into the device and experiencing simultaneous enhancement from the same excitation source, but different extracted wavelengths. The resulting pixelated surface on a flexible substrate enables blending of the color and directional output of multiple QD emission

wavelengths for potential lighting or display applications.

CHAPTER 3

POLARIZATION CONTROLLED OUTPUT OF ELECTROHYDRODYNAMIC JET PRINTED QUANTUM DOT EMBEDDED PHOTONIC CRYSTALS

Tailored optical output, such as color purity and efficient optical intensity, are critical considerations for displays, particularly in mobile applications. To this end, we demonstrate a replica molded photonic crystal structure with embedded quantum dots. Electrohydrodynamic jet printing is used to control the position of the quantum dots within the device structure. This results in significantly less waste of the quantum dot material than application through drop-casting or spin coating. In addition, the targeted placement of the quantum dots minimizes any emission outside of the resonant enhancement field, which enables an 8X output enhancement and highly polarized emission from the photonic crystal structure.

3.1 Introduction

Lighting and display applications require color purity and tailored control of the optical properties of their output. For example, the directivity or diffusivity of a light source affects user comfort and the viewing angle of displays, while color purity determines display fidelity. Polarization is particularly crucial, as it affects contrast and power efficiency in many display devices, such as liquid crystal displays, which have a backlight that is immediately passed through a polarizer, and use transmittance filters to provide spectral control for the output [140].

Quantum dots (QDs) have been investigated as a potential replacement for phosphors in lighting applications, and as a means to improve color rendering in light-emitting diode (LED) based lighting and display

Material in this chapter is reprinted, with permission, from G. See et al., "Polarized quantum dot emission in electrohydrodynamic jet printed photonic crystals," *Applied Physics Letters*, vol. 107, pp. 051101, August 3, 2015.

applications [65, 72]. QDs offer good color saturation and purity, a capacity for solution-based processing and greater stability than many phosphors [65, 72, 141] and these properties make them appealing for lighting [134, 142] and display [71] applications.

Due to high fabrication costs, there is significant interest in improving the performance and efficiency of QDs within devices. Embedding QDs within photonic crystals (PCs) offers a promising route towards increasing optical excitation efficiency, while simultaneously improving the emitted photon collection efficiency through PC-enhanced extraction [83, 138, 143]. The resonant conditions of a PC can be tuned to wavelengths ranging from the infrared [36, 144] to the UV [130] through the appropriate design selection of the grating dimensions and refractive indices of the materials used. In addition, PCs can be designed to affect the polarization [145] and output directionality [56, 79] of photon emitters embedded within them.

In PC slabs, resonant modes occur when specific phase matching conditions of the angle and wavelength of incident light are met, allowing light to couple in and out of leaky guided resonance modes [22, 146]. Light coupling to the PC excites a localized electromagnetic standing wave with significantly larger amplitude than that of the original source. Emission that occurs in the same spectral and physical region of this evanescent field region will couple to the guided modes of the PC, resulting in outcoupling along the phase matching angle. Because the transverse-electric (TE) and transverse-magnetic (TM) polarizations occur at different resonance conditions, it is also possible to use PCs as polarizers [19, 22].

In 1D and 2D PC slabs that serve as a quasi-planar device structure upon which QD-infused thin films can be readily applied, the optical coupling between PCs and QDs requires that the QDs reside within the resonant evanescent electric field volume, which decays exponentially away from the PC surface [82]. The evanescent field of a PC resonator extends from the PC surface and decreases to $1/e$ of the peak value at a depth ranging from 10-50% of the resonant wavelength. Therefore, for QDs designed to emit in the visible part of the optical spectrum, QDs should be located within a few hundred nanometers of the PC surface if they are to experience enhanced excitation and enhanced extraction. Methods used to apply QD-doped polymer thin films to PCs must therefore be capable of producing film thicknesses in the 10-500 nm range.

For QDs embedded within the evanescent electric field region of a PC, emission is polarized along preferred orientations from the PC [147]. Polarized emission has been observed for QDs embedded within dielectric optical resonators as well as plasmonic structures [148, 149]. As described previously, many types of display devices require a polarizer over the backlight that results in a loss of at least 50% of the optical efficiency of the display [140]. Both liquid crystal [150] and LED-based [151] backlight displays have sought to polarize the light emission through more efficient means.

Nanoreplica polymer molding has been used to create PCs that contain QDs embedded in a UV-curable polymer thin film [83]. In such a structure, one approach for applying the QD-doped polymer thin film is spin-casting, which results in substantial waste of QDs, because only a small fraction of the QD/polymer material is incorporated into the resulting thin film, while the remaining material is cast into the spinner bowl lining.

Electrohydrodynamic jet (E-jet) printing is a recently developed approach for highly controlled spatial and volumetric deposition of liquids onto a variety of planar and non-planar surfaces. E-jet printing uses a voltage difference between the printing nozzle and the substrate to create consistent, high resolution printed patterns [152–154]. E-jet printing has been used for semiconductor fabrication [155], biological sensing [156], and micro-optical devices [152]. QD-embedded polymer structures have been fabricated with ink jet printing for display applications [157] but E-jet printing is also capable of printing with multiple nozzles [152, 158] and achieves finer resolution than ink jet printing, with features as small as 240 nm to 10 μm and linewidths as narrow as 25 nm [153, 154, 159–161]. In this work, an uncured polymer containing a QD solution was printed over a specified region for replica molding, eliminating the wasted and unenhanced QDs in the polymer layer of a PC.

In this work, we demonstrate QD-embedded PCs fabricated through E-jet printing of a UV curable polymer onto a replica molding master, and subsequent transfer to a substrate that supports the finished device structure. The QDs are placed inside the regions with the greatest the electric field magnitude within the PC structure, resulting in a higher photon output than is produced without the PC structure. In addition, the targeted placement of the QDs to be in close proximity to the PC grating

minimizes any QD emission outside the resonant evanescent field volume. This enables highly polarized output emission, due to the significantly higher enhancement present for photons oriented to interact with the transverse magnetic (TM) mode of the PC. The approach described and demonstrated in this work offers the potential to double the energy efficiency for display devices that utilize a polarized backlight by eliminating the optical power lost through a polarizing filter, while simultaneously providing an 8X enhancement in the QD emission output intensity.

3.2 Device Structure

The PC structure, shown in Figure 3.1(a), consists of a linear grating formed by replica molding a polymer doped with QDs. The polymer mixture is E-jet printed over a master, shown in the SEM images in Figure 3.1(b) and (c), where the grating has a pitch of Λ=340 nm with a 67% duty cycle and a depth d=120 nm. As illustrated in Figure 3.1(d), the printed structure is transferred to a plastic substrate and a high refractive index layer of TiO_2 (t=105 nm) is deposited over the surface of the polymer grating to create the periodic variation in the refractive index of the device.

The PCs were designed with the aid of electromagnetics simulation software (Lumerical FDTD) to enhance QD emission at one selected wavelength in the visible region of the spectrum (λ=575 nm). The photonic band structure was modeled and is shown in Figure 3.1(e) as a function of the angle and wavelength, with the TE and TM polarizations specifically identified at normal incidence. The darker bands indicate the locations of resonance conditions where the wavelength and angle are capable of coupling to the PC. The electric field intensity for both the TM and TE polarizations at λ=575 nm excitation were modeled and a comparison is shown in Figure 3.2. The simulations show identical cross sections of the PC grating, with a 3X greater intensity for the TM polarization than the TE polarization.

The structure of the device consists of several discrete PC regions arranged to form a block figure, shown in the SEM of the device in Figure 3.1(b). The PC regions may be as small as 40 μm, but up to 320 μm, on a side. It is also possible for the device to include regions that contain

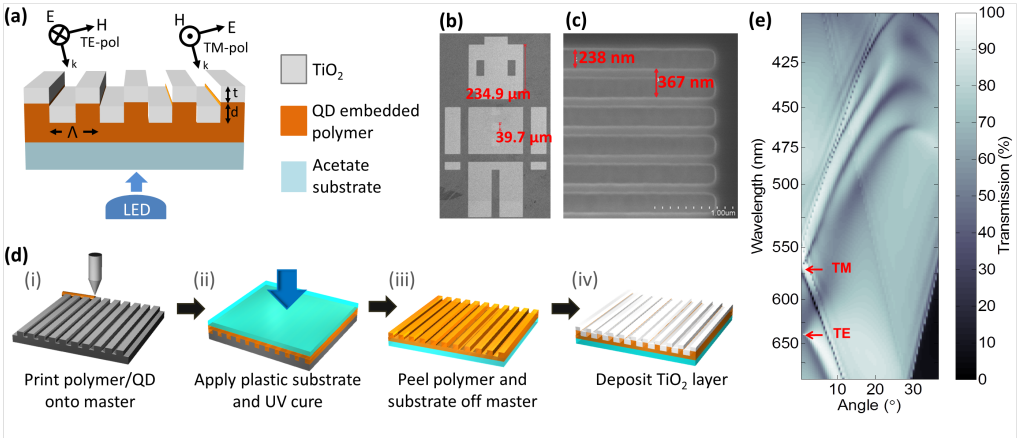

Figure 3.1: (a) A schematic cross section of the device structure, consisting of a replica molded polymer layer on a flexible plastic substrate with a TiO_2 film deposited over the top surface. The resulting photonic crystal has a transverse-electric (TE) polarization parallel to the linear grating, while the transverse-magnetic (TM) polarization is perpendicular to the grating. The QDs in the polymer layer are excited by collimated light from an LED. SEM images of (b) the replica molding master, from which features as small as 40 m were replicated with E-jet printing, and (c) the PC grating at higher magnification. (d) The PC fabrication process described in the Materials and Methods Section consists of (i) E-jet printing the QD-embedded polymer over the silicon master, (ii) applying the plastic substrate and curing the polymer, (iii) peeling off the replica from the master and (iv) depositing the TiO_2 film over the cured polymer. (e) The simulated band structure of the PC grating. The dark bands indicate the phase matching conditions for the angle and wavelength of light at which resonances occur within the PC.

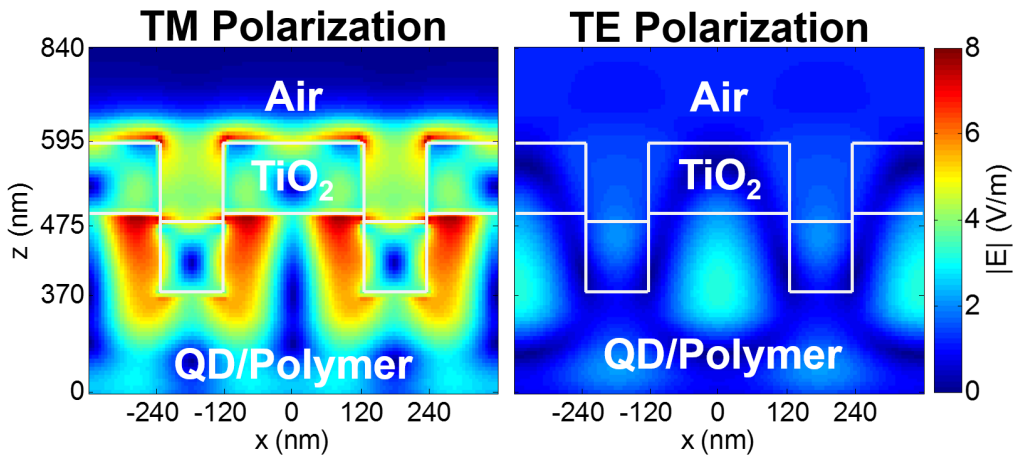

Figure 3.2: Field distributions of two periods of the photonic crystal simulated using finite-difference time-domain analysis under excitation at λ=575 nm by TM (left) and TE (right) polarizations.

another distinct grating structure in which the PC grating may run either parallel or perpendicular to the grating of the other regions.

The PCs were designed with the aid of electromagnetics simulation software (Lumerical FDTD) to determine the PC dimensions necessary for a structure with TM polarized resonance conditions that overlap with QD emission at one selected wavelength in the visible region of the spectrum (λ=575 nm) as a demonstration. Simulations were performed using the refractive index values across the visible spectra, but with particular interest at the target wavelength λ=575 nm, using the RI values of TiO_2 (n=2.625) [139] and the UV curable polymer (n=1.524, Woolam VAS Ellipsometer). Both the TM and TE polarizations at λ=575 nm excitation were modeled and a comparison of the electric field intensity is shown in Figure 3.2. The simulations show a clear difference in the intensity of the grating cross sections under the different polarization conditions.

3.3 Materials and Methods

To fabricate the devices, a replica molding master, shown in Figure 3.1(b) and (c), was patterned using electron beam lithography on a silicon wafer with a layer of thermally grown SiO_2. Reactive ion etching (PlasmaLab Freon/O_2 Reactive Ion Etcher System) was then used to etch the 120 nm

deep trenches for the grating. The master was cleaned with piranha etch and coated with 1H,1H,2H,2H-Perfluorooctyltrichlorosilane (No-Stick from Alfa Aesar) before the polymer was E-jet printed onto the surface.

The state of the silicon surface has a large impact on the quality of the printing process. If the wafer surface is too hydrophobic, the printed droplets scatter instead of forming continuous lines. If the surface is too hydrophilic, the cured polymer is difficult to delaminate from the master. The use of No-Stick provides the appropriate hydrophobicity for repeatable E-jet printing.

To prepare the QD-doped polymer solution, two monomers, 91 μL of Lauryl methacrylate (LMA, Sigma-Aldrich) and 9 μL of ethylene glycol dimethacrylate (EGDMA, Sigma-Aldrich) were mixed in a flask, followed by the addition of 4 mL of CdSeS/ZnS alloyed QDs in a toluene solution (Sigma-Aldrich). The remaining solvent was evaporated using a rotary evaporator and then 1 v% Darocur 1173 (Sigma-Aldrich) initiator was added to the mixture. The resulting QD-LMA solution was used for printing.

The polymer grating is formed by E-jet printing the solution over the silicon master, followed by curing the polymer layer (Figure 3.1(d)). The printing used a gold/palladium (Au/Pd) coated nozzle dipped in a hydrophobic coating of 0.1% (by weight) dimethylformamide with a tip diameter of 5 μm, which allowed the QD-LMA solution to be printed continuously without clogging the nozzle. The printing voltage and speed were optimized to form continuous lines on the PC substrate. By pre-programming the printing process through the E-jet interface, specific areas and sizes could be printed automatically.

After printing, the substrate was transferred into an argon atmosphere glove box and cured under UV illumination for 30 min. AFM measurements (Digital Instruments Dimension 3000 Atomic Force Microscope) show that the thickness of this layer is 600 nm, which is a significant decrease in thickness as compared to the 8 μm thick layer produced by spin-casting the same material (Dektak 3030 profilometer). Another layer of LMA solution, this time without any QDs, was drop-cast on the substrate and covered with a Grafix acetate substrate. After the second LMA layer was fully cured, the two-layer film was peeled away from the master. Finally, a layer of high refractive index TiO_2 was deposited over the patterned polymer-QD

structure, which converts the structure into a photonic crystal.

The device performance was characterized using the collimated output of a UV LED (Thor Labs, Ultra Bright Deep Violet LED) with a center wavelength of λ=375 nm and a 20 nm full-width half-maximum as the excitation source. The UV emission was also passed through a $350< \lambda <390$ nm bandpass filter to ensure that only the UV wavelengths interacted with the QDs in the device. The device output was measured by mounting the PC device on a motorized rotation stage with control of the orientation in 0.1° steps, allowing the output emission of the device to be measured over a viewing angle range of ±20°. The output was passed through a UV filter and collected by a collimating lens on an optical fiber connected to a USB2000+ Ocean Optics spectrometer. The stage position and collected emission data were controlled by a custom LabView OmniDriver software interface.

The same setup was also used to measure the transmission through the device by replacing the UV LED with a collimated, unpolarized broadband tungsten-halogen lamp as the source. In this case, the QDs are not excited, and the photonic band diagram of the PC can be determined instead. The same angle range was tested to compare the band diagram with the measured emission.

3.4 Results

The device was initially measured after the grating was fabricated with the QD doped polymer, but before the TiO_2 deposition, to provide a baseline measurement for the output emission intensity. The measurements were repeated after the TiO_2 deposition. As shown in Figure 3.3, at the center wavelength of λ=575 nm, there is an 8X enhancement in the output intensity. The inset shows a tight angular dependence of ±2.5° for the PC enhancement at the target wavelength.

The enhanced emission is also polarized. Figure 3.4(a) shows the modeled and measured transmission spectra of the device. The measured transmission shows dips in the unpolarized transmission spectra occurring at wavelengths of λ=575 nm and 620 nm, as predicted by the model for the TM and TE modes, respectively. However, the measured transmission

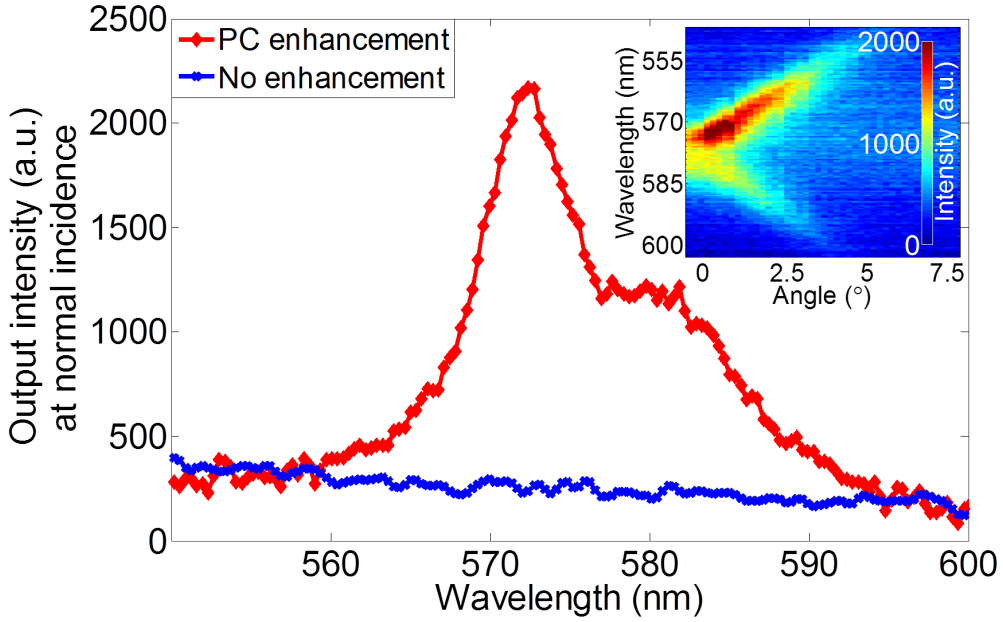

Figure 3.3: An 8X enhancement in the output intensity occurs with the presence of the PC structure over the QD embedded polymer structure. The inset shows the angle dependence of the QD emission and enhancement from the PCs.

values are significantly larger than those predicted by the model. This is because the active device region is only 7.75% of the total substrate area that was measured, and the large inactive region contributed a significantly higher transmission to the measurement than occurs for the PC alone. The measured QD emission is shown for both the TM and TE polarizations in Figure 3.4(b) and (c), respectively, where a polarizer has been added between the device and the measurement collection optics. The TM output intensity is 5X greater than the TE, and the TE output is comparable to the noise floor of the measurement system.

3.5 Discussion

The E-jet printing process allows for precise placement of QDs on the PC patterned regions, to fabricate devices that show an 8X enhancement in output intensity. This capability is important in the context of creating a surface that contains an array of PCs in the form of red-green-blue emitting

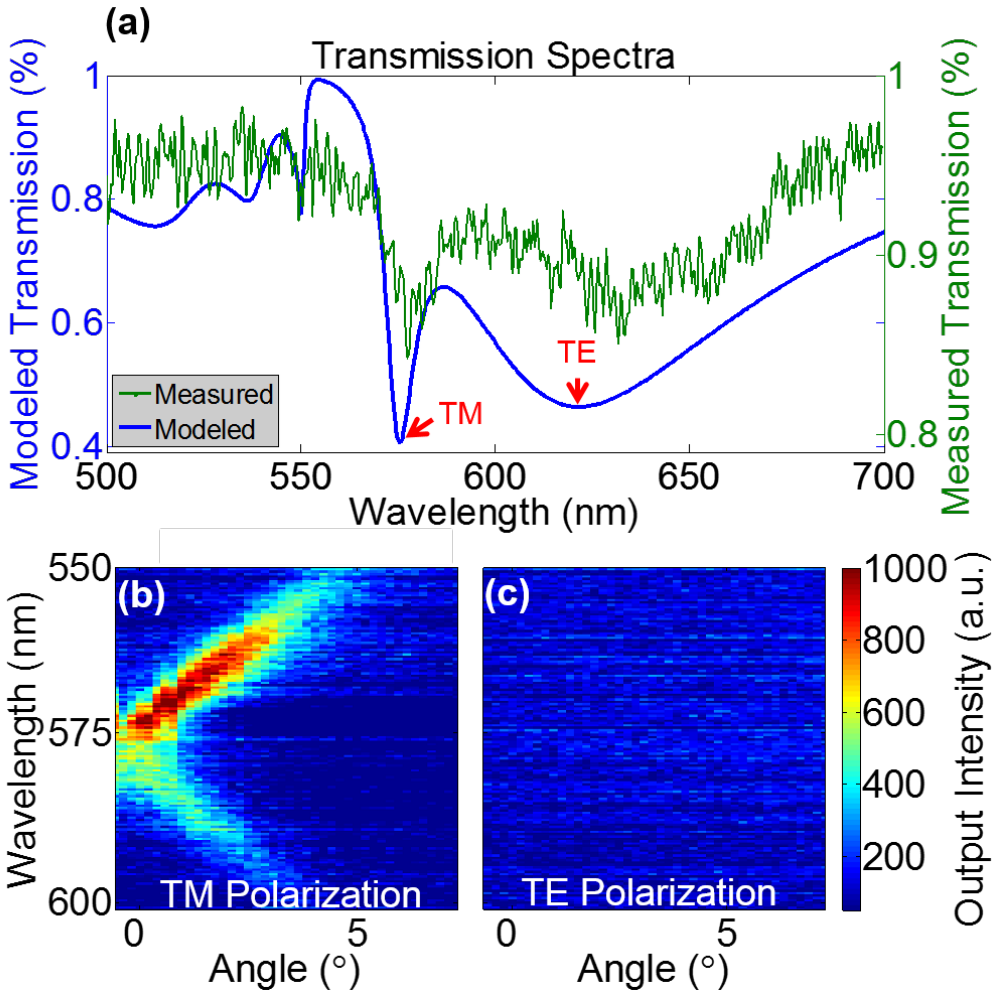

Figure 3.4: (a) The modeled and measured transmission spectra of the photonic crystal at normal incidence, and the measured (b) TM and (c) TE polarized output from the PC figure. The TM polarized output demonstrates enhancement, while the output of the TE polarization is comparable to the measured background. Because the TE polarization of the PC is offset by λ=45 nm, there is no overlap with the TM mode, and thus no output enhancement of the QDs, creating an on/off mechanism for the QD output from the PC.

pixels, where individual PC regions may be optimized for a specific wavelength of QD emitter that would be selectively printed upon them. Figure 3.5 shows a fluoresence microscope image of the E-jet printed device. The top inset shows the clean edges printed by the system over the device regions. The bottom inset shows a duller edge where the printing was not perfectly aligned with the PC region. The fainter regions occur where there is no PC enhancement of the QD emission and show a clearly visible contrast in brightness between the planar region and the 8X enhancement provided by the PC structure, thus verifying the enhancement effect of the PC.

The cost improvements offered by the use of E-jet printing are substantial. The precise placement of the QDs eliminates the waste of spin-casting or loading QDs into device regions where there is no need for emitters. In addition, the 600 nm film thickness, compared to the 8 μm thick layer produced with spin-casting, concentrates the emitters in the high enhancement regions of the photonic crystal and reduces the required volume of QD/polymer solution for the film by over 90%. There are minimal regions in which the QD emitters experience no enhancement and this drastically increases the total emission efficiency.

3.6 Conclusions

Creating initially polarized backlighting with selected color regions, as enabled by the targeted placement and polarized output of these structures, will enable significant improvements in the energy efficiency of display devices, which is critically important for displays incorporated within mobile devices. By eliminating the backlight polarizer in a display, the optical efficiency can be doubled, and eliminating color filters can triple the efficiency. These improvements are all combined with scalable production by nanoreplica molding and the use of flexible plastic substrates, which enable an array of novel device platforms.

Future improvements for the devices include the use of QDs that can be excited with a non-UV source. In addition, increasing the printing speeds and printing red-green-blue specific device regions would improve the viability for scalable display production. If coupled with thin film

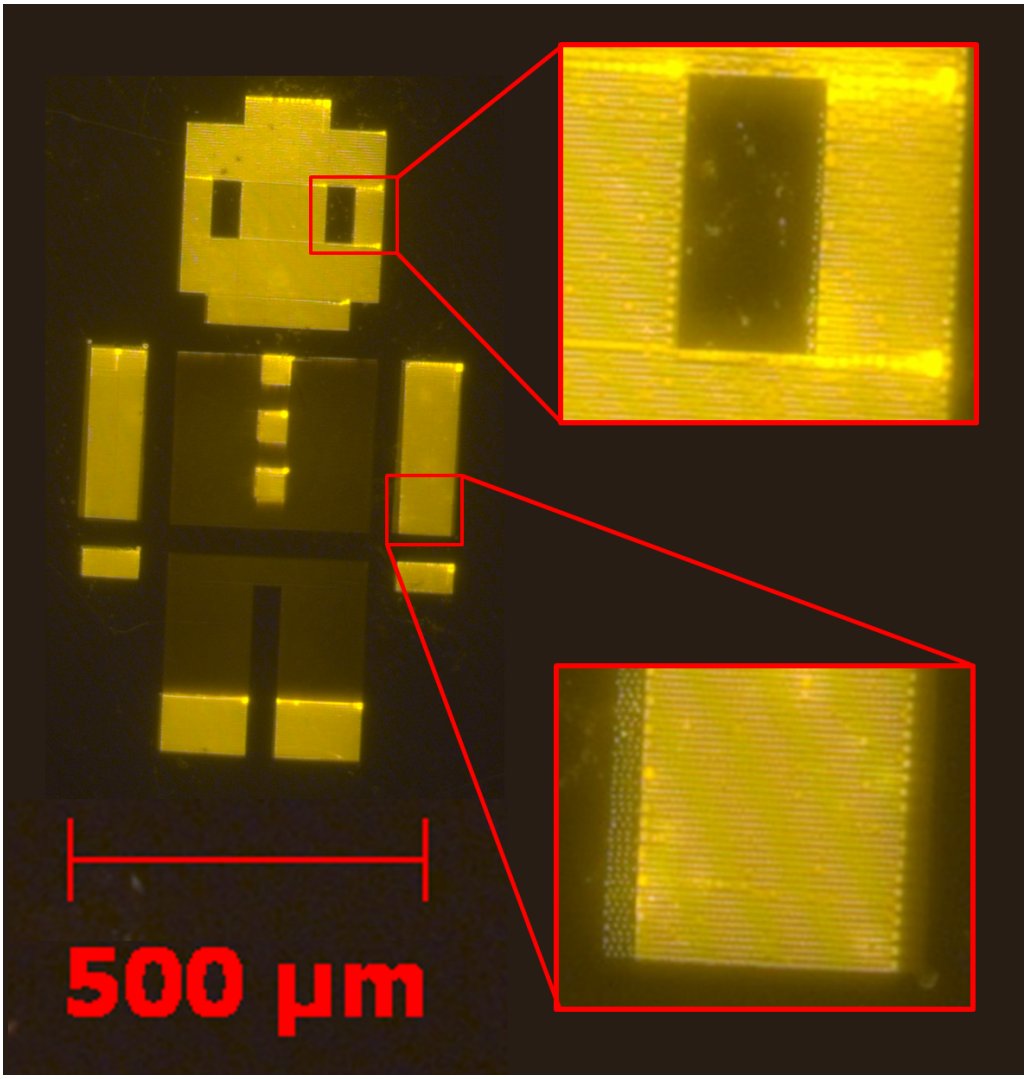

Figure 3.5: A fluoresence microscope image of the E-jet printed device. The top inset shows the sharpness of the edges printed by the system. The bottom inset shows a duller edge where the printing was not perfectly aligned with the replica molding master. The fainter regions are due to QD emission occurring in a planar region with no PC structure to provide enhancement.

transistors for switching, then E-jet printed PC regions would provide pixelated control of color and polarization for use in screen displays for computers, televisions and other devices that require the high color purity of QDs.

The devices in this work demonstrate the precise placement of QDs within specific regions of replica molded PCs, using a scalable fabrication method. The devices show both polarized emission and an 8X increase in output intensity, as compared to output emission without the PC structure. These improvements have the potential to eliminate polarizers from backlight display technology and double their optical efficiency. Through the controlled placement of QDs, the E-jet fabrication methodology decreases the wasted QD material by more than 90% from spin- and drop-casting techniques for identical device areas. These cost and performance improvements are key advances toward overcoming the barriers to cost-effective QD display technology.

CHAPTER 4

ENHANCED EMISSION OF QUANTUM DOTS EMBEDDED WITHIN THE HIGH-INDEX DIELECTRIC REGIONS OF PHOTONIC CRYSTAL SLABS

We demonstrate a method for combining sputtered TiO_2 deposition with liquid phase dip-coating of a quantum dot (QD) layer that enables precise depth placement of QD emitters within a high-index dielectric film, using a photonic crystal (PC) slab resonator to demonstrate enhanced emission from the QDs when they are located at a specific depth within the film. The depth of the QDs within the PC is found to modulate the resonant wavelength of the PC as well as the emission enhancement efficiency, as the semiconducting material embedded within the dielectric changes its spatial overlap with the resonant mode.

4.1 Introduction

Since their introduction by Yablonovitch [33], photonic crystals (PCs) have been adopted for a broad range of applications that include optical filters [22], biosensors [162], and photodetectors [36]. In addition to passive optical components, PCs have proven to be useful within light emitting devices, where their dispersion can be used to increase the efficiency of photon extraction from light emitting diodes (LEDs) [50, 56, 58, 163] or to enhance the excitation intensity of embedded photon emitters such as fluorescent dyes or quantum dots (QDs) [80, 81, 137, 143].

Photon-emitting devices that contain QDs are gaining importance for applications in lighting and video display due to their high quantum efficiency, lack of photobleaching, and availability of many emission wavelengths that can be combined to engineer a specific overall spectral output. However, due to the high fabrication cost of QDs in comparison to conventional phosphors, it is highly desirable to utilize them efficiently through development of device structures that can optimally place them

within regions where their output is optimally extracted.

The structure of a PC consists of a periodic variation of high and low refractive index materials. Through appropriate design choices for the feature sizes and material properties, it is possible to tune the optical and electromagnetic properties to enable a wide range of applications. In particular, when a PC is designed to operate as a guided mode resonant filter, regions of increased energy density within the structure at the resonant wavelength can be used to amplify the excitation power experienced by photon emitters that are located within the electromagnetic field standing wave.

In this work, we demonstrate a fabrication approach that enables QDs to be incorporated within a narrow cross section of the high-index dielectric thin film and within the spatial volume of an optical standing wave mode of the PC resonant slab. The QDs experience greater electric fields for excitation from their electronic ground state, and are also optimally placed so that their emission can be extracted most efficiently in the direction normal to the PC slab surface [82]. We use a novel method to apply a distinct, monolayer-scale film of QDs, and show that judicious placement of the QD "slice" within the high-index dielectric film is necessary to optimize the enhanced extraction factor. In addition, we show an increase of 3-5X greater QD emission from within a PC, as compared to the intensity measured from a QD layer that is not embedded within a PC. This emission enhancement is as high as 8X for off-normal output angles.

There are numerous applications that have benefited from embedding QDs within dielectric materials. Dielectric microcavities can provide mode control of QD emission [164] and the spontaneous emission from QDs can be controlled by embedding them in dielectric spheres of varying radii [165, 166]. The incorporation of QDs into dielectric materials has also been used for charge storage in metal-oxide-semiconductor capacitors [167] and electronically erasable programmable read only memory (EEPROM) [168] for data storage applications.

Devices with distinct 30300 nm thick QD layers have been fabricated by ion beam sputtering [169], ion implantation [168], or spin coating onto sputtered thin films, often with a matrix material [134, 164, 170]. QDs can modify the dielectric susceptibility of the material they are embedded in [171], and improve both absorption and photoelectric performance of

photoelectrodes and solar cells when layered with TiO_2 [168, 169, 172, 173]. Silicon QDs embedded within a variety of amorphous matrix materials (silicon oxide, silicon nitride and silicon carbide) have been shown to impact the effective refractive index of their host material, producing both blue and red shifts in the optical absorption spectra of the matrix material [169, 174].

For many embedded QD devices that are used in lighting or video display applications, controlled placement within the structure is crucial to achieving optimal output intensity performance. For example, in early devices demonstrating nanocrystals in LEDs, the nanocrystals were layered with organic spacers to control their position [175]. Within PCs, the QD positioning is a crucial aspect of the excitation and output emission efficiency, determining how much of the QD emission is coupled to the PC resonant modes.

4.2 Device Design and Structure

In PCs excited at their resonant wavelength, the electric field intensity decays exponentially with increasing distance from the surface [82], making it desirable to keep emitters close to the structure surface or embedded within the device itself. To this end, we demonstrate a method that combines sputter deposition of dielectric material with liquid-phase dip-coating of QDs to create PCs with an embedded QD layer. The refractive index of the dielectric TiO_2 layer is altered by the presence of the QD layer, while the output efficiency of the QDs is highly dependent upon the depth of the QDs within the dielectric layer.

The device structure consists of two distinct 2D PC regions that enable side-by-side comparison of QD emission intensity from regions that either match or mismatch the PC resonant wavelength with the emission wavelength of embedded QDs. As shown in Figure 4.1(a), the regions are interleaved in a checkerboard format, in which alternating regions have distinct resonance wavelengths. Each region has two orthogonal periods, as shown in the inset, and the two periods are designed to enhance both the excitation and emission wavelengths of embedded QDs [176].

For example, the 2D-PC in Region 1 of the checkerboard has a short period (L=200 nm, 40% duty cycle) in the x-direction and a longer period

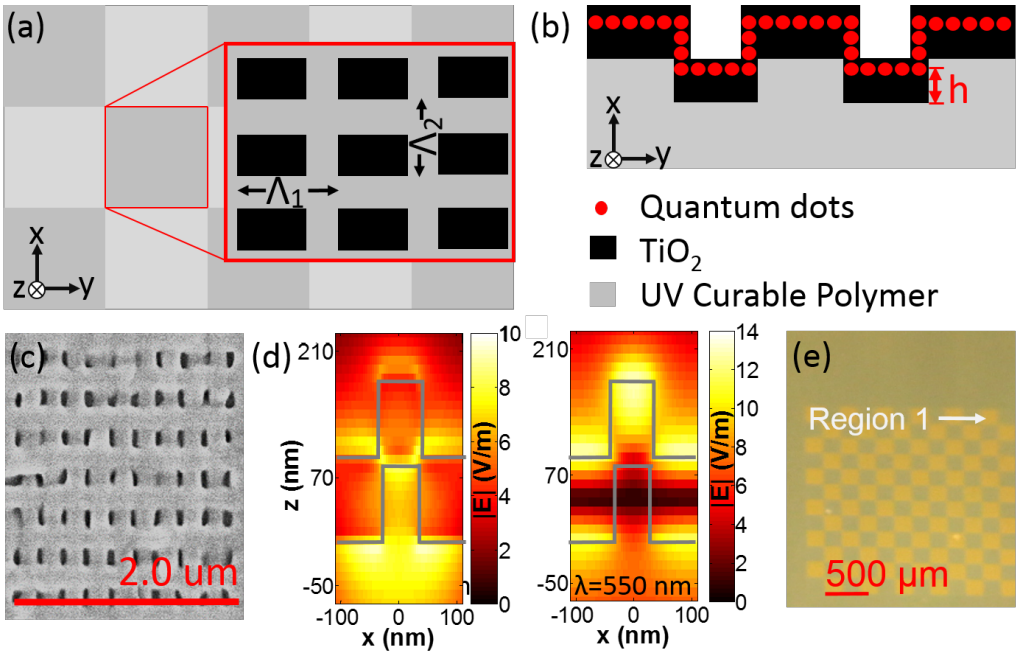

Figure 4.1: (a) A top view of the device structure, consisting of two interleaved regions with different PC periods in the x and $y-$directions. (b) A cross-section schematic of the PC with QDs embedded in the TiO_2 dielectric layer. (c) An SEM image of the PC region designed to enhance QD emission at λ=615 nm. (d) Modeled electric field intensities for the PC at λ=615 nm (left) and λ=550 nm (right), illustrating that both the wavelength and location of the QDs within the electric field will affect the enhancement conditions. (e) A photograph of QDs embedded in the checkerboard PC structure, where the orange locations show regions of enhanced emission (Region 1), while the QD emission in Region 2 and the surrounding bulk area is not enhanced.

(L=340 nm) in the y-direction. The short period is designed to produce a guided mode resonance at the UV wavelengths of $350 < \lambda < 390$ nm used for QD excitation, while the longer period is designed to produce a resonance at the λ=615 nm wavelength of QD emission.

Region 2 of the checkerboard has a short period of L=200 nm (70% duty cycle) in the x-direction and a long period of L=250 nm in the y-direction, where the short period is also designed to produce a guided mode resonance at the QD excitation wavelength, but the long period produces a resonance at a wavelength of λ=480 nm. Therefore, when QDs with an emission wavelength centered at λ=615 nm are embedded within the entire structure, all the QDs (in both parts of the checkerboard) will be excited

with a resonant enhancement effect, but only QDs within Region 1 will participate in the enhanced extraction effect.

Finite difference time domain electromagnetic computer simulation (Lumerical, FDTD) was used to determine that a 95 nm thickness of TiO_2 (n=2.35, Metricon Model 2010/M Prism Coupler) layer would optimize coupling to unpolarized QD emission at λ=615 nm. This was consistent with values extrapolated from the resonance conditions in previous PC devices fabricated using the same grating structure but alternate deposition thicknesses of the TiO_2 layer [176].

The region with a resonance targeted to enhance the λ=615 nm QD emission has a 340 nm period with a 60% duty cycle and an orthogonal grating with a period of 140 nm with a 70% duty cycle. The alternate PC checkerboard region has an optical resonance at a shorter wavelength of λ=490 nm, but it does not overlap with the QD emission, and halves the effective device area providing QD emission enhancement. The difference in output intensity is visible to the naked eye and enables a visual confirmation of QD enhancement, as shown in the photograph of a QD embedded PC in Figure 4.1(e). To simplify this study, the optical characteristics near the λ=615 nm resonance are the focus of the results presented in this work.

As shown in Figure 4.1(b), the PC has a replica molded polymer grating structure over which a specific thickness, h, of TiO_2 is deposited. A layer of QDs is then applied by dip-coating over the TiO_2 surface, and the remainder of the desired TiO_2 thickness is deposited over the QDs. An SEM image of the top surface after the final TiO_2 deposition is shown in Figure 4.1(c).

The modeled electric field for resonant modes at λ=615 nm and λ=550 nm are shown in Figure 4.1(d), demonstrating that the location of the peak electric field intensity changes with the incident wavelength within the same PC structure. By varying the depth of the QD emitters within the TiO_2 layer, we anticipate that enhancement of the QD emission intensity will also vary. To investigate the impact of the QD placement within the TiO_2 region, we fabricated devices with the configurations described in Table 4.1, with each batch consisting of three PC samples and a flat control sample that was created with the same procedure, but without the periodic grating structure.

Table 4.1: The fabrication parameters for TiO_2 and QD layers for each batch of test structures.

Batch	Layer 1	Layer 2	Layer 3	Layer 4
1	Replica molded polymer	30 nm TiO_2	QD	65 nm TiO_2
2	Replica molded polymer	60 nm TiO_2	QD	35 nm TiO_2
3	Replica molded polymer	90 nm TiO_2	QD	5 nm TiO_2

4.3 Materials and Methods

Photonic crystal (PC) fabrication utilizes a master silicon wafer containing a negative image of the desired replica molded structure for the PC grating. The mold consists of a thermal oxide SiO_2 layer with electron beam lithography (JEOL JBX-6000FS) patterning to produce 80 nm pillars with reactive ion etching (PlasmaLab Freon/O_2 Reactive Ion Etcher). The etched area was cleaned for 20 min with a solution of piranha etchant (3:1 (v/v) mixture of sulfuric acid and hydrogen peroxide), then rinsed with de-ionized water, dried with N_2 and treated for 1 hr with a vapor phase deposition of (tridecafluoro-1,1,2,2-tetrahydrooctyl) trichlorosilane (No-Stick, Alfa Aesar) in a closed container with two drops of No-Stick solution. The post etch processing enables the consistent removal of the replica from the master wafer.

The replica molded layer of the PC was formed with a UV curable polymer that contained 91 μL of Lauryl methacrylate (LMA) and 9 μL of ethylene glycol dimethacrylate (EGDMA) mixed in a flask, followed by the addition of 1 μL of initiator (Darocur 1173, Sigma-Aldrich). The solution was drop-coated onto the master wafer, and covered by a sheet of Optigrafix Acetate, that had been previously treated with a vapor phase deposition of 3-(trimethoxysilyl)propyl methacrylate (Sigma Aldrich) to increase the polymer adhesion. The droplet spread and formed a continuous thin layer between the silicon substrate and acetate sheet. It was polymerized under a high intensity UV lamp for 30 min in an argon atmosphere, and then the film containing the replicated grating structure attached to the acetate substrate and could be removed from the master.

Sputtering was used to deposit the desired thickness of the high refractive index TiO_2 layer (K. J. Lesker Dual-Gun Sputter System) over the replica molded polymer layer. A cadmium selenide (CdSe) quantum dot (QD) dip

coating solution was synthesized with an oleic acid ligand coating, purified twice by precipitation and centrifugation with ethanol and methanol, and then redispersed in hexane at the original concentration. The PC was dipped into the solution for 15 sec, removed and allowed to dry for at least 5 min. If the deposition was not uniform, the PC could be soaked in hexane to remove the quantum dots and the dipping procedure would be repeated. Finally, hexane was used to remove QDs from the back surface of the substrate to eliminate any confounding emission outside the PC device area. Additional sputtering was then performed to complete the TiO_2 layer.

The test setup used to characterize the output of each test structure is operated by a LabVIEW OmniDriver interface. The excitation source for the QDs is a collimated UV light emitting diode (Thor Labs, Ultra Bright Deep Violet LED) with a center wavelength of λ=375 nm. The LED has a full-width, half-maximum of 20 nm and a $350 < \lambda < 390$ nm bandpass filter was also used to eliminate any non-UV wavelengths from reaching the structure under test and interfering with the measurement of the QD emission. For testing, the structure is mounted on a motorized rotation stage, which allows for 0.1° step increments in the orientation of the structure's surface to the optical axis of the test setup. The output emission at each position was collected after passing through a UV filter and collimating lens on an optical fiber, and then analyzed by a USB2000+ Ocean Optics spectrometer.

By using a broadband, unpolarized tungsten-halogen lamp as the source (replacing the LED and bandpass filter), the transmission spectra through the structures could also be measured. The illumination source was passed through a bulk sample that had experienced identical processing to the photonic crystal test structure, providing a control measurement for light attenuation through the various layers. Identical measurements were then taken of the test structures, and normalized with the control measurements, to determine the photonic band structures and the angular dependence of the output emission.

4.4 Results and Discussion

The minimum value of the measured transmission efficiency at normal incidence was used to determine the reported wavelength of the resonance mode. The modeled transmission efficiency for a continuous TiO_2 dielectric layer, shown as the black line in Figure 4.2, was normalized for the 50% effective area of the checkerboard pattern used for comparison with the measured transmission spectra.

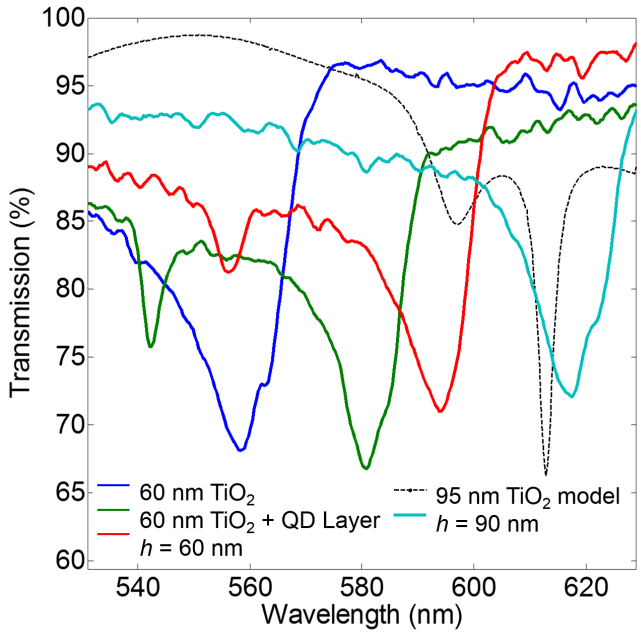

Figure 4.2: The normalized transmission efficiency spectra of the PCs at various stages of fabrication and the modeled transmission spectra normalized for the 50% effective area of the checkerboard device. The largest dip is the resonance mode that is intended to couple with the QD emission, although additional resonances are present in the structure, which are observed as shallower dips in the transmission spectra. The addition of a QD layer results in a resonance shift of λ=20-25 nm and disrupts the continuous electric field within the dielectric layer, causing a change in the measured resonance conditions of the final device structure, as compared to the modeled results.

As shown in Figure 4.2, each layer of deposited TiO_2 material caused a red-shift in the transmission efficiency minimum. There was also a shift of $\lambda = 20 - 25$ nm caused by the addition of the QDs observed in every sample. For those structures with the QDs added at h=90 nm, with only 5

nm of TiO_2 deposited over the QD layer, the transmission efficiency minimum occurred at λ=620 nm. This minimum occurs at a wavelength only $\Delta\lambda$=5 nm greater than λ=615 nm value predicted by the modeled results for a continuous dielectric layer with no embedded QDs. However, for the other device conditions, after the final TiO_2 layer was deposited over the QDs the resonance wavelengths for the other depths h are blue shifted from the modeled wavelength by $\Delta\lambda$=40 nm for h=30 nm and by $\Delta\lambda$=15 nm for h=60 nm.

In these PCs, the continuous refractive index of the TiO_2 layer is disrupted and the effective refractive index of the PC is altered by the higher refractive index material of the QDs (n=2.5-2.64, depending on size [177, 178]). The impact of the QDs on the refractive index varies with their location within high or low intensity portions of the electric field, further modifying the effective refractive index of the photonic crystal. Thus, this finding is consistent with both the blue [174] and red [169] shifts in refractive index observed for QD embedded dielectrics in previous studies.

The output intensities of the fabricated devices were also measured across a range of angles, and the impact of the QD location within the dielectric layer in relation to the enhancement of the QD emission was determined. Because the resonance is dependent on both the extraction angle and wavelength of the light coupling out of the PC, the output intensity, as shown in Figure 4.3, was measured across a range of angles from normal incidence 0° to 20° at the peak QD emission of λ=615 nm. The output intensity was averaged for the three PC structures measured in each experimental condition. The enhancement factor was determined by dividing the average QD output intensity within the PC by the planar control structure output intensity for each experimental condition. The actual enhancement factors for the checkerboard regions with a resonance matched to the emission wavelength of the QD will actually be 2X higher than the values we report here, because the QD emission in the alternate checkerboard regions are not enhanced.

Figure 4.3 clearly shows that the depth of the embedded QDs within the dielectric layer of photonic crystals impacts the enhancement of the QD emission. The highest enhancement factor at normal incidence was 5X and occurred in the structure with a QD layer closest to the TiO_2 surface,

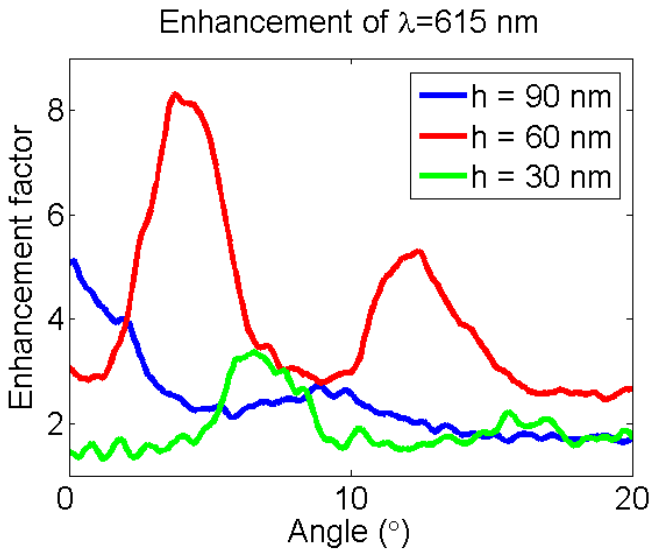

Figure 4.3: The PC-enhanced output of QD emission at λ=615 nm, as compared to planar structures with identical fabrication steps. The location of the QD layer in the structure affects both the intensity and angular output of the measured emission. The largest enhancement occurred for QDs embedded at h=60 nm within the TiO_2 layer; however, the only enhancement factor at normal incidence occurred at h=90 nm.

placed at a depth h=90 nm. This is expected from the modeled results for λ=615 nm light extracted at normal incidence, shown in Figure 4.1(d), where the greatest electric field is concentrated along the top surface of the high refractive index layer. However, other fabricated structures demonstrated higher enhancement factors (up to 8X) at an extraction angle of 4° for QDs placed at h=60 nm of TiO_2, and 7° for QDs at h=30 nm.

The varied angle at which the peak enhancement occurs indicates that the depth placement of emitters within PCs can be used to control both the intensity and angular output of emitted photons. This methodology would be useful to simultaneously enhance multiple QD emission wavelengths embedded at different locations within the PC structure and create tailored lighting outputs. Placement of QDs at multiple depths could also be used to specifically control the angular output of specific wavelengths, creating wide angle viewing that is desirable for screens and shared displays, or a targeted, narrowly angled output to provide privacy or depth perception for the viewer.

4.5 Conclusions

Using the dip-coating procedure presented in this work, we have demonstrated that varying the location of QD emitters within the high refractive index region of a PC structure can be used to tailor the enhancement and extraction angle of emitted photons. The peak enhancement values range from 3X-8X, depending on both the depth of the QD placement and the extraction angle of the photonic crystal coupled emission. In addition, the depth of the embedded QDs affects the effective refractive index of the dielectric PC layer and thus the enhancement factors produced by the device, adding a new design parameter that must be considered early in the design process in order to produce the desired output enhancements.

CHAPTER 5

PHOTONIC CRYSTALS ON ACOUSTIC MEMS RESONATORS

5.1 Introduction and Background

Display technology is a major power consumer, particularly in mobile applications. Performance is characterized by its polarization, directionality, color spectrum and intensity. Quantum dots (QDs) are semiconductor crystals that downconvert light and produce a very narrow bandwidth emission which provides for high color fidelity in displays. This makes them highly desirable emitters, but due to the cost of producing high quality QDs, there is significant interest in increasing the efficiency of QD emission in devices and reducing the quantities required.

One method for controlling and enhancing QD emission is through the use of photonic crystals (PCs). Photonic crystals are structures with periodic variation in their refractive index. The materials and dimensions of the PC structure determine the resonance conditions of the grating. In the case of a linear grating this consists of the period, duty cycle, and thickness of the layers.

Resonance conditions occur at specific wavelength and angle combinations, creating a localized electromagnetic standing wave in the structure. Emitters can be placed within the localized field and experience a much higher electric field intensity than is present in the source, which allows emitters to experience enhanced excitation. In addition, there is an enhanced extraction mechanism. As light couples in and out of the PC at resonance conditions, light collected at the outcoupling angle for the appropriate wavelength will be higher intensity than the isotropic emission occurring from an emitter outside of a resonant PC structure.

PC structures have successfully demonstrated enhanced spectral output intensity for ultraviolet to infrared wavelengths [79, 137, 176, 179], angular

control of output [55, 180, 181] and polarized output [182, 183]. Coupled with the spectral quality of QDs for displays, they are a powerful combination for improved display technology. However, most PCs are static structures, providing a constant interaction with the light sources they couple to. An active PC structure would enable PC enhancement to be turned on and off, as demonstrated in [183], where the presence of a photonic crystal increased light emission to a visually detectable threshold.

Numerous methods have been investigated to tune the resonance of a photonic crystal. An externally applied electric [89, 90] or magnetic field [91, 92] can be used to adjust the refractive index of PC materials. Applied stress or strain to change the period of the PC features has been successfully demonstrated to shift the photonic bandgap of PC devices [96, 97], while extensive modeling of mechanical strain has shown theoretical potential [98–102].

A similar approach to tuning is through the use of piezoelectric materials. In this case, an applied voltage is used to induce a mechanical displacement in the PC structure. Piezoelectric control of PCs has been investigated for several device architectures. Strain tuning quantum dot coupling to a PC cavity red-shifted emission by 0.45 nm; however, an applied voltage of 15 kV/cm was required [109]. A one-dimensional PC that was mounted on piezoelectric actuators produced a resonance shift of 1.54 nm [110]. A PC of self-assembled polycarbonate on a piezoelectric substrate of polyvinylidene fluoride demonstrated an infrared bandgap, although tuning was not demonstrated [111].

Additional piezoelectric tuning methods for PCs have been proposed. These include a hexagonal air hole array in a silicon matrix over a piezoelectric substrate requiring 3% applied shear strain to result in 75% exclusion of the original bandgap [114]. Another proposed device consists of a 1D Bragg stack and uses a surface acoustic wave to shift the refractive index n of the material layers, and thus the reflection and transmission of the device [115].

For our purpose of PC enhanced emission, piezoelectric tuning is an appealing methodology as it limits any confounding interaction with the QDs or other emitters. It allows for external control of switching and the voltage control provides very specific displacement, making tuning control more precise. Using DC piezoelectric bias requires a driving voltage on the

order of kV to produce enough displacement to shift the PC resonance away from the emission peak of QDs; however, AC resonators have much larger displacements. If the AC signal is faster than the 60 Hz flicker sensitivity of the human eye, the modulation will not be detectable to viewers [11].

In particular, bulk acoustic wave (BAW) resonators provide a large displacement across a significant portion of the surface area of the device, key parameters for piezoelectrically driven displacement of a photonic crystal.

5.2 Device Design and Structure

The device, shown in Figure 5.1 is based on a standard bulk acoustic wave resonator, with a 1 μm thick piezoelectric layer of aluminum nitride (AlN) sandwiched between 100 nm platinum electrodes. There is an additional 1 μm layer of AlN over the top electrode with the PC grating and a UV curable polymer containing the QDs. This structure is released from the substrate during fabrication, leaving it suspended over a cavity and free to resonate.

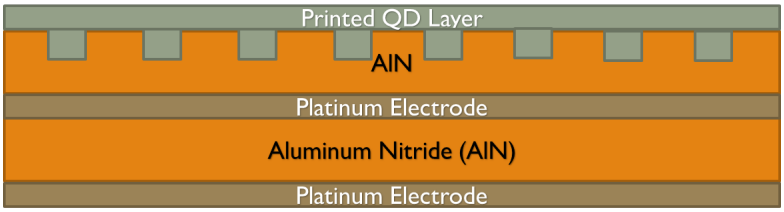

Figure 5.1: The structure of the piezoelectric MEMS resonators. A piezoelectric AlN layer is sandwiched between Pt electrodes, and an additional AlN layer is added over the electrodes with a PC grating. The PC is completed with a printed layer of UV curable polymer and embedded quantum dots.

Resonators were simulated using finite element analysis (Comsol Multiphysics 5.1, Piezoelectric module) to determine the optimal dimensions and corresponding resonance frequencies of the devices. A maximum in the admittance indicates a resonant frequency of the device. The surface average function was used to determine which devices and resonant frequencies provide the largest average displacement values at the

surface of the top AlN layer. An example of displacement and admittance modeling results is shown in Figure 5.2, where the resonant frequencies correspond to the frequencies at which the average surface displacement is at a maximum.

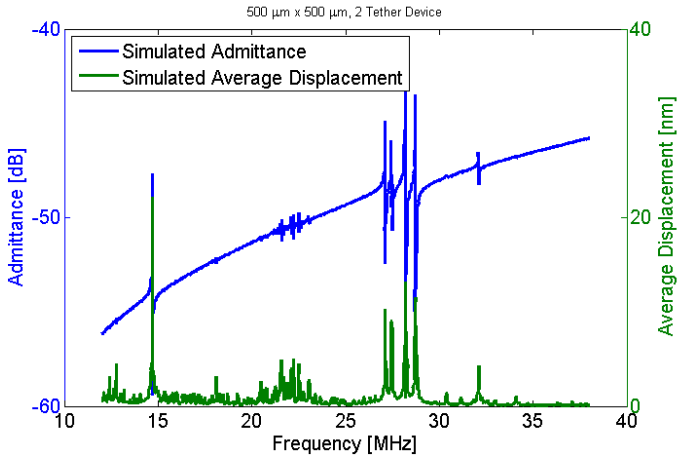

Figure 5.2: Simulated admittance and surface average displacement for a 500 μm x 500 μm device. The peak average displacement values correspond to the resonant frequencies indicated by maximum values in the admittance.

A variety of dimensions ranging from 150 μm to 500 μm were simulated. Resonators with two centered tethers or four tethers (one on each corner) with the same resonator body dimensions were also simulated. These devices were important because of concerns that the multiple AlN layers would be too heavy to be supported by the two tether design. The displacements of two simulated devices, both 400 μm by 300 μm, are shown at resonance in Figure 5.3, where (a) has two center tethers, and (b) is simulated with four corner tethers.

A list of the devices that were simulated and fabricated, along with their modeled resonant frequencies and corresponding maximum average displacement values, is shown in Table 5.1.

The PC grating is patterned into the top AlN layer on the resonator. By adjusting the period of a PC grating, the resonant wavelength will be shifted and the magnitude of the electric field within the PC at that wavelength will decrease. The electric field for an aluminum nitride (AlN) grating covered by a layer of UV curable polymer with embedded CdSe quantum dots was determined using finite difference time domain simulations (Lumerical FDTD).

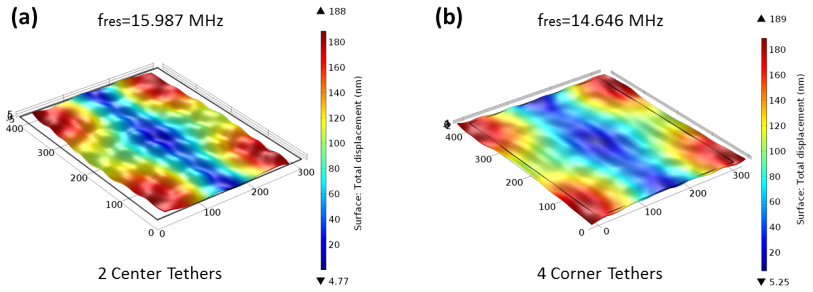

Figure 5.3: The simulated displacement of two resonators at resonance is shown. Both are 400 μm by 300 μm, where **(a)** is simulated with two centered tethers and **(b)** with four tethers, one at each corner.

The selected QDs have an emission centered at λ=540 nm with a full-width at half maximum of λ=30 nm. The optimal design for enhancement at that wavelength consists of a 175 nm deep grating with a 350 nm period and a 600 nm thick polymer layer. A range of grating periods were simulated, as shown in Figure 5.4, to confirm that the electric field for both increasing and decreasing displacements would be much lower than that of the "static" condition. Depending on the displaced grating period, the electric field intensity at λ=538 nm is decreased by 62-79%.

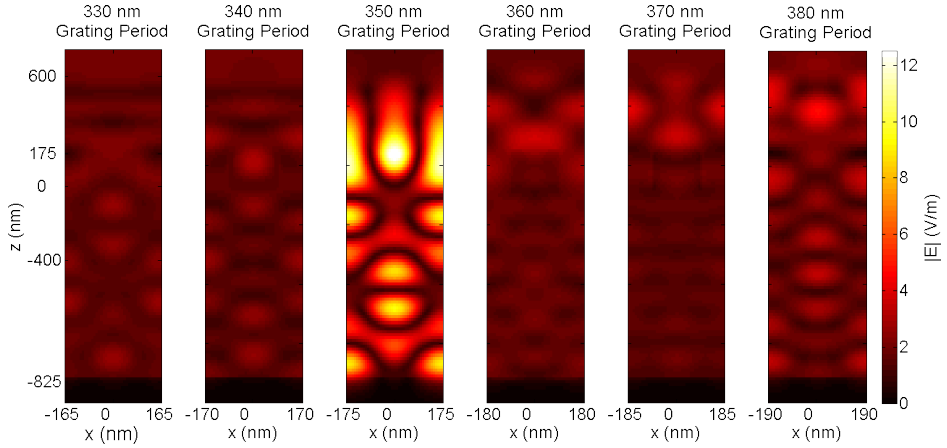

Figure 5.4: Simulated electric field intensity at the center wavelength of the QD emission (λ=538 nm) for different grating periods. By increasing or decreasing the grating period at least 10 nm, the electric field enhancing the QD emission is reduced by 62-79%.

5.3 Fabrication

The MEMS-PC devices were fabricated on a high resistivity silicon substrate. The bottom electrodes were evaporated onto the surface (CHA SEC-600 Electron Beam/Thermal Evaporator), then the AlN layer was reactively sputtered (OEM Group). The Pt/AlN layer deposition was repeated for the second electrode and the AlN PC layer.

Electron beam lithography (JEOL JBX-6000FS) was used to pattern the PC grating, which was etched using inductively coupled plasma reactive ion etching (Oxford Instruments PlasmaLab System 100 ICP RIE) with a gas mix of BCl_3, Cl_2, and Ar in a 1:4:4 ratio. Photolithography was used to pattern the electrical vias and resonator release windows, which were separated into 1 μm and 2 μm deep features and etched using the same RIE process as for the PC grating.

Once the AlN layer was removed from the Si wafer substrate, the resonators were released with a XeF_2 etch (XACTIX XeF_2 Etching System). A QD-doped polymer solution was prepared using two monomers, consisting of 91% Lauryl methacrylate (LMA, Sigma-Aldrich) and 9% ethylene glycol dimethacrylate (EGDMA, Sigma-Aldrich). CdSeS/ZnS alloyed QDs in a toluene solution (Sigma-Aldrich) were added, with the amount depending on the desired concentration of QDs. Remaining solvent was evaporated using a rotary evaporator and 1 v% Darocur 1173 (Sigma-Aldrich) initiator was added.

This solution was printed using a microinjector system that allows for nL volumes to be dispensed on the resonator surfaces. Finally, the QD/polymer solution was cured under UV to complete the devices. It is important that the printing takes place after the resonator release, as the XeF_2 gas can permeate the cured polymer. It will etch the QDs and cause significantly reduced QD emission. The fabrication process is illustrated in Figure 5.5.

Completed devices were tested on an RF probe station. A network analyzer (Agilent N5230A PNA-L Network Analyzer) was used to sweep each device and determine the resonant frequencies at which to drive the devices. After characterization, a UV source (ThorLabs 370E UVLED) was passed through a 350 nm$< \lambda <$390 nm filter to eliminate any non-UV wavelengths, and the output was aligned over the QD printed resonator to excite QD emission. An optical fiber was mounted over the device under

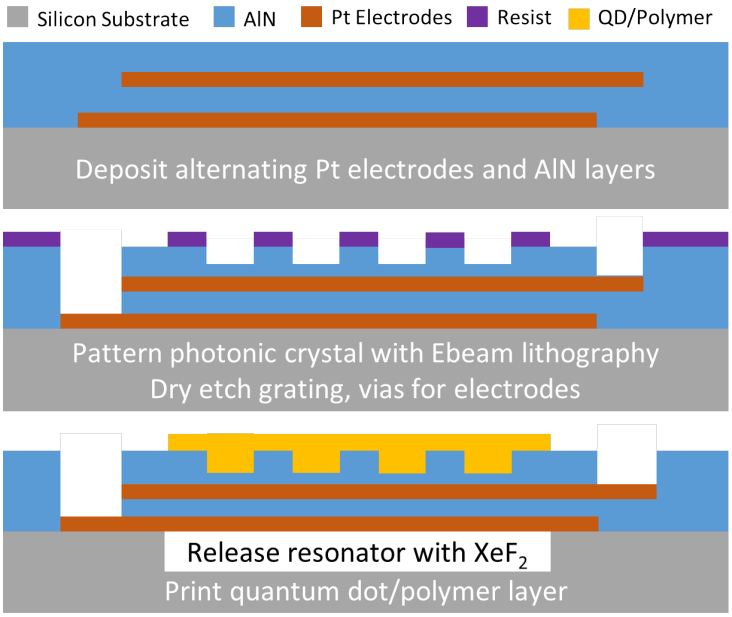

Figure 5.5: The fabrication process used to produce the PC MEMS devices. The Pt electrodes and AlN layers were deposited on a high resistivity Si wafer. The PC grating, electrical vias, and release windows were etched using reactive ion etching. Finally, the resonators were released using a XeF_2 etch to remove the Si beneath the device and the QD/polymer solution was printed and cured on the resonator surface.

test, and aligned by adjusting position until the output measured by the connected photodetector (ThorLabs DET36) was at its peak. The output of the photodetector was measured by an oscilloscope (Agilent DSO 1614A). A signal generator (Agilent N5181A MXG Analog Signal Generator) was used to apply a signal at the resonant frequency to the device. Using a splitter, this signal was also measured by the oscilloscope.

5.4 Results and Discussion

The PNA frequency sweep to determine resonance conditions was compared to the modeled admittance characteristics. The devices were swept at two different powers, 1 dBm and 5 dBm, to verify resonant frequencies would be consistent with higher driving power. Admittance characteristics changed slightly with power, with resonances at 5 dBm generally having a lower quality factor and, at frequencies below 20 MHz, often producing spurious

modes, decreasing the performance of some devices. The plotted comparison for a 400 μm x 300 μm device is shown in Figure 5.6. The simulated and measured characteristics for additional devices are listed in Table 5.1.

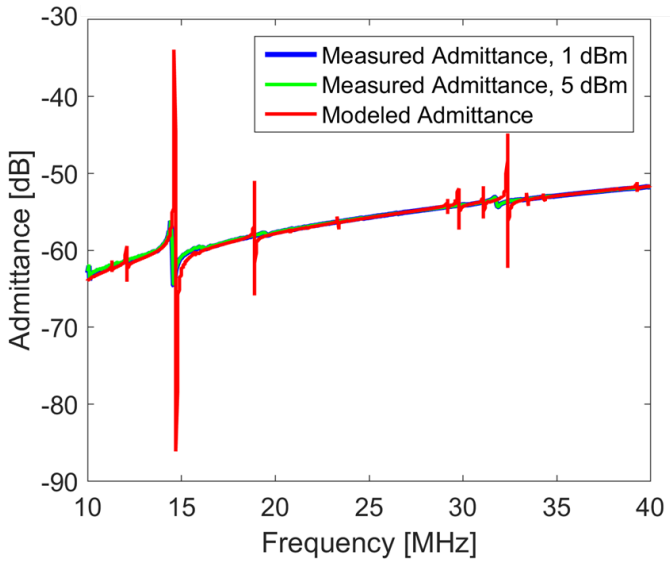

Figure 5.6: A comparison of the modeled and measured impedance characteristics. The quality factors of the measured impedances are lower than in the model, and thus not all resonance frequencies appear in the measured output; however, the frequency location of measured resonances is within 0.5-1 MHz of the modeled location for the majority of devices.

For devices with lengths less than 500 μm, the measured resonance frequencies match the simulations very closely; however, the quality factors are lower on the measured devices. This is due to slight misalignments during lithography steps, causing non-uniform sidewalls, and to damping if the QD/polymer layer is printed unevenly. Devices 500 μm and longer showed a greater mismatch between the simulated and measured impedance values. This is due to residual strain in the AlN film.

The measured QD emission from devices were compared to the driving RF signal and to control outputs from the device with no modulation. Output signals had poor signal-to-noise ratios, due to the short detection time on 10-30 MHz signals and the rise speed (14 ns) of the photodetector. To improve output quality, signals were averaged over 248-1024 measurements.

The 500 μm x 350 μm device with two tethers showed effective

modulation of the QD emission at a 23.84 MHz driving signal and the modulation was not present when the RF driving signal was turned off. The measurements are shown in Figure 5.7. During modulation, the outcoupling direction of the PC changes for the QD emission wavelength, and the amount of emission collected normal to the device surface by the optical fiber tip varies. Without the driving RF signal, the PC structure is static and the outcoupling of QD emitted light by the PC is constant.

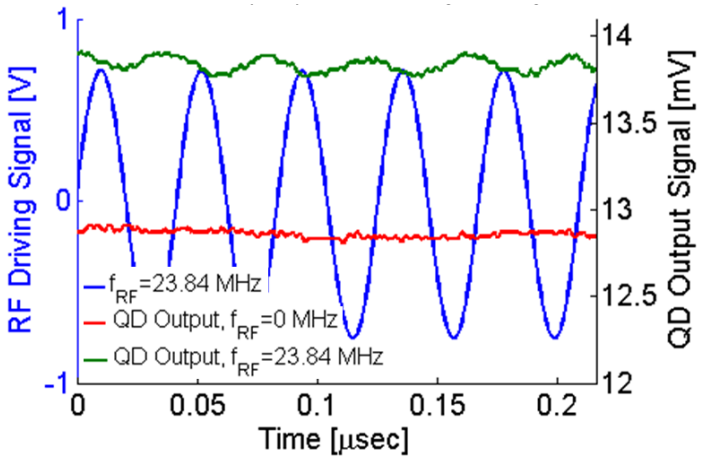

Figure 5.7: Measured oscilloscope signals from a 350 μm x 500 μm device with two tethers. The QD emission output varies with the driving RF signal. When the driving signal is turned off, the emission is a DC signal.

Because of the noise, a Fourier transform was performed on the measured signal data to confirm the modulated QD emission from the devices. Figure 5.8 shows the Fourier transform applied to the measurements from the 500 μm x 350 μm device shown in Figure 5.7. Figure 5.8(a) contains a peak at 23.84 MHz for the RF source and the modulated QD output from the device. As the frequency of the source signal is increased to 25.03 MHz, the power measured from the QD emission at the modulation frequency drops sharply, indicating that the PC is deforming less effectively away from the MEMS resonance and is outcoupling QD emitted light at lower intensity. The device demonstrated this same behavior at a lower frequency resonance of 12.18 MHz, again with the power of the QD emission signal decreasing with a slight change of the modulation frequency, as shown in Figure 5.8(b).

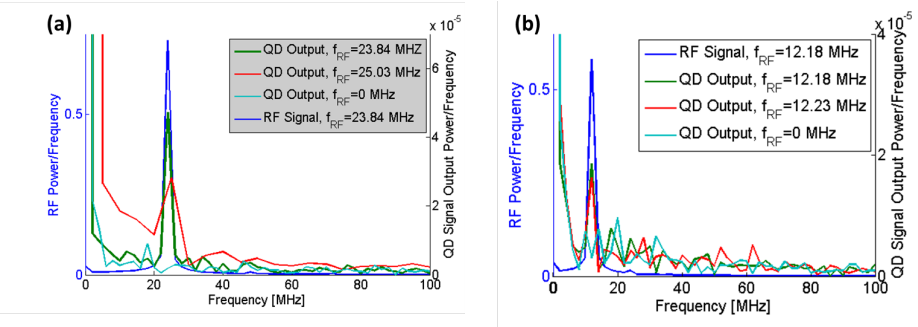

Figure 5.8: A Fourier transform was applied to the time domain output signals of the RF source and the modulated PC out-coupled QD emission. For a 500 μm x 350 μm device, there is a resonance frequency at (a) 23.84 MHz and (b) 12.18 MHz. In both cases, the QD emission from the device shows a peak at the frequency of the RF driving signal. As the driving signal increases away from the resonance frequency, the power from the QD emission decreases, indicating that the modulation of the PC is less effective away from the device resonance frequency.

5.5 Conclusions and Future Work

Piezoelectrically tuned PC enhancement structures can be produced with CMOS compatible fabrication methods already used for thin-film transistors (TFTs) in existing display technology; however, future devices would benefit from decreased area required to release the resonator for better integration with existing display device architecture. A possible method is to use a DC bias, but this requires more exotic piezoelectric materials at the cost of processing ease and compatibility.

The integration of a photonic crystal onto a piezoelectric MEMS resonator has successfully demonstrated modulation of light emission from QDs embedded within the PC structure. The efficacy of the modulation is highly dependent on the dimensions of the resonator, as this impacts the directionality and uniformity of the PC displacement over the surface of the device. The PC-MEMS devices presented leverage the enhancement mechanisms of PCs for improved QD emission and have the potential to offer pixel level control of output emission in next generation display devices.

Table 5.1: Key simulated and measured values for resonators, where **L** is the resonator length, **W** is the resonator width, **D** is displacement, and f_r is a resonant frequency.

L [μ**m**]	**W** [μ**m**]	**Tethers**	f_r [**MHz**]*	**D** [**nm**]*	f_r [**MHz**]†	Q†
225	150	2	31.613	47.872	28.783	872.02
225	225	2	22.787	86.824	21.487	364.69
400	300	2	15.987	103.71	14.644	518.06
400	300	4	14.65	104.90	14.47	72.85
400	350	2	14.05	103.71	12.65	327.57
400	400	2	12.813	128.37	11.522	148.42
400	450	4	11.138	149.79	11.020	61.887
			30.78	12.774	29.254	199.72
500	350	2	13.600	100.77	12.206	369.99
			26.293	15.991	23.856	512.49
500	400	2	12.093	139.32	11.256	228.13
500	450	2	15.427	23.847	10.175	516.39

* Simulated value

† Measured value

CHAPTER 6

CONCLUSIONS AND FUTURE WORK

With lighting being one of the top uses of power in today's homes and workplaces, improved efficiency and spectral characteristics in lighting and display technology have the potential to significantly impact global power consumption, and provide a more consumer friendly method of lower power, high fidelity lighting for home use. Such improvements can also provide increased device performance, particularly in mobile applications.

PCs with embedded QDs have successfully shown improvement over a range of capabilities. Through the use of distinct periods in orthogonal directions, 2DPCs can be used for simultaneous enhancement of the excitation and extraction wavelengths of QDs. Adjusting the location of emitters within the structure allows for variable enhancement factors and resonance conditions within the PC. Linear gratings also provide enhanced spectral intensity and control. These different device structures have produced enhancement factors ranging from 2-12X.

Region specific control, particularly relevant to pixel-level device integration, has been demonstrated through multiple means. Replica molding masters can be fabricated with interleaved distinct PC regions, allowing for simultaneous enhancement of different emitters with their own extraction wavelengths. Electrohydrodynamic jet printing produces sub-micron area control when placing QDs within a PC structure, as well as allowing for extremely thin layers of QD-doped polymer to be produced.

Beyond dramatically reducing the required quantities of QD materials for fabrication, producing QD-embedded films of specific thickness enables polarized output emission from the QD-PC structure. If integrated into existing LCD display structures, the use of a polarized source can more than double the optical efficiency of displays.

Finally, actively modulating QD emission has been accomplished by integrating PCs onto BAW resonators. By leveraging the piezoelectric

displacement occurring in these resonators, the PC will be actively deformed, changing the angle and wavelength of resonantly outcoupled light.

By building on these capacities for enhancement and control, it is possible to develop next generation lighting and display technology. Pixel scale integration of polarization, enhancement, and modulation are huge enablers for future display technology. In addition, the use of replica molding for PC fabrication can broaden the available platforms for both lighting and displays.

Photonic crystal enhanced QD emission provides an excellent device architecture for leveraging the high quality spectral characteristics of QDs for lighting and display technology and decreasing production costs through increased performance and efficiency. QD-embedded PC devices have demonstrated improvements to the key metrics of display performance: polarization, directionality, and output intensity through multiple methods for enhancing and controlling the output intensity of QD emission.

REFERENCES

[1] "Energy efficiency: A compelling global resource," McKinsey Sustainability & Resource Productivity, Tech. Rep., 2010.

[2] B. W. D'Andrade and S. R. Forrest, "White organic light-emitting devices for solid-state lighting," *Advanced Materials*, vol. 16, no. 18, pp. 1585–1595, 2004.

[3] "Laboratory evaluation of light-emitting diode (LED) T8 replacement lamp products," U.S. Department of Energy, Lighting Design Lab, Pacific Northwest National Laboratory, Seattle, Washington, Tech. Rep. May, 2011.

[4] J. Herrman, "Ultimate light bulb test: Incandescent vs. compact fluorescent vs. LED," *Popular Mechanics*, 2012. [Online]. Available: http://www.popularmechanics.com/technology/gadgets/tests/incandescent-vs-compact-fluorescent-vs-led-ultimate-light-bulb-test

[5] M. A. Baldo, S. Lamansky, P. E. Burrows, M. E. Thompson, and S. R. Forrest, "Very high-efficiency green organic light-emitting devices based on electrophosphorescence," *Applied Physics Letters*, vol. 75, no. 1, pp. 4–6, 1999.

[6] P. E. Burrows, G. Gu, V. Bulovi, Z. Shen, S. R. Forrest, and M. E. Thompson, "Achieving full-color organic light-emitting devices for lightweight, flat-panel displays," *IEEE Transactions on Electron Devices*, vol. 44, no. 8, pp. 1188–1203, 1997.

[7] S. Bae, H. Kim, Y. Lee, X. Xu, J.-S. Park, Y. Zheng, J. Balakrishnan, T. Lei, H. R. Kim, Y. I. Song, Y.-J. Kim, and K. S. Kim, "Roll-to-roll production of 30-inch graphene films for transparent electrodes," *Nature Nanotechnology*, vol. 5, no. August, pp. 1–5, 2010.

[8] R. Mertens, "Samsung announces Super AMOLED plus displays," 2011. [Online]. Available: http://www.oled-info.com/samsung-announces-super-amoled-plus-displays

[9] "Energy savings potential of solid-state lighting in general illumination applications," Navigant Consulting, Inc. for Solid State Lighting Program, U.S. Department of Energy, Washington, DC, Tech. Rep. January, 2012.

[10] D. Yokoyama, "Molecular orientation in small-molecule organic light-emitting diodes," *Journal of Materials Chemistry*, vol. 21, pp. 19 187–19 202, 2011.

[11] S. J. Williamson and H. Z. Cummins, *Light and Color in Nature and Art*. John Wiley & Sons, Inc, 1983.

[12] D. Bozyigit and V. Wood, "Challenges and solutions for high-efficiency quantum dot-based LEDs," *MRS Bulletin*, vol. 38, no. September, pp. 731–736, 2013.

[13] Z. Luo, D. Xu, and S.-t. Wu, "Emerging quantum-dots-enhanced LCDs," *Journal of Display Technology*, vol. 10, no. 7, pp. 526–539, 2014.

[14] J. D. Joannopoulos, S. G. Johnson, J. N. Winn, and R. D. Meade, *Photonic Crystals, Molding the Flow of Light*, 2nd ed. Princeton: Princeton University Press, 2008.

[15] R. W. Wood, "On a remarkable case of uneven distribution of light in a diffraction grating spectrum," in *Proceedings of the Physical Society of London*, vol. 18, London, 1902, pp. 269–275.

[16] A. Hessel and A. A. Oliner, "A new theory of Wood's anomalies on optical gratings," *Applied Optics*, vol. 4, no. 10, pp. 1275–1297, 1965.

[17] M. Neviere, P. Vincent, R. Petit, and M. Cadilhac, "Systematic study of resonances of holographic thin film couplers," *Optics Communications*, vol. 9, no. 1, pp. 48–53, 1973.

[18] A. Hessel and A. A. Oliner, "Wood's anomaly effects on gratings of large amplitude," *Optics Communications*, vol. 59, no. 5,6, pp. 327–330, 1986.

[19] S. S. Wang, R. Magnusson, and J. S. Bagby, "Guided-mode resonances in planar dielectric-layer diffraction gratings," *Journal of the Optical Society of America A*, vol. 7, no. 8, pp. 1470–1474, 1990.

[20] L. F. Desandre and J. M. Elson, "Extinction-theorem analysis of diffraction anomalies in overcoated gratings," *Journal of the Optical Society of America A*, vol. 8, no. 5, pp. 763–777, 1991.

[21] D. Rosenblatt, A. Sharon, and A. A. Friesem, "Resonant grating waveguide structures," *IEEE Journal of Quantum Electronics*, vol. 33, no. 11, pp. 2038–2059, 1997.

[22] R. Magnusson and S. S. Wang, "New principle for optical filters," *Applied Physics Letters*, vol. 61, no. 3, pp. 1022–1024, 1992.

[23] R. Magnusson, Y. Ding, K. J. Lee, D. Shin, P. P. Young, and T. A. Maldonado, "Photonic devices enabled by waveguide-mode resonance effects in periodically modulated films," in *SPIE Nano- and Micro-Optics for Information Systems*, L. A. Eldada, Ed., vol. 5225. Bellingham, WA: SPIE, 2003, pp. 20–34.

[24] F. Yang, "Energy transduction in surface photonic crystals," Ph.D. dissertation, University of Illinois at Urbana-Champaign, 2009.

[25] J. Hu and C. R. Menyuk, "Understanding leaky modes: slab waveguide revisited," in *Advances in Optics and Photonics*. Optical Society of America, 2009, ch. 1, pp. 58–106.

[26] K. M. Ho, C. T. Chan, and C. M. Soukoulis, "Existence of a photonic gap in periodic structures," *Physical Review Letters*, vol. 65, no. 25, pp. 3152–3155, 1990.

[27] K. M. Leung and Y. F. Lui, "Full vector wave calculation of photonic band structures in face-centered-cubic dielectric media," *Physical Review Letters*, vol. 65, no. 21, pp. 2646–2649, 1990.

[28] H. Y. Ryu, Y. H. Lee, R. L. Sellin, and D. Bimberg, "Over 30-fold enhancement of light extraction from free-standing photonic crystal slabs with InGaAs quantum dots at low temperature," *Applied Physics Letters*, vol. 79, no. 22, p. 3573, 2001.

[29] A. Pokhriyal, M. Lu, V. Chaudhery, C.-S. Huang, S. Schulz, and B. T. Cunningham, "Photonic crystal enhanced fluorescence using a quartz substrate to reduce limits of detection," *Optics Express*, vol. 18, no. 24, pp. 24 793–24 808, 2010.

[30] B. A. C. Edrington, A. M. Urbas, P. Derege, C. X. Chen, T. M. Swager, N. Hadjichristidis, M. Xenidou, L. J. Fetters, J. D. Joannopoulos, Y. Fink, and E. L. Thomas, "Polymer-based photonic crystals," *Advanced Materials*, vol. 13, no. 6, pp. 421–425, 2001.

[31] J.-C. Cotteverte, B. A. Eid, and C. F. P. Renvaze, "Active photonic crystal waveguide device," Patent 6,542,682, 2003.

[32] B. Temelkuran, S. D. Hart, G. Benoit, J. D. Joannopoulos, and Y. Fink, "Wavelength-scalable hollow optical fibres with large photonic bandgaps for CO_2 laser transmission," *Nature*, vol. 420, no. December, pp. 650–653, 2002.

[33] E. Yablonovitch and T. J. Gmitter, "Photonic band structure: The face-centered-cubic case," *Physical Review Letters*, vol. 63, no. 18, pp. 1950–1953, 1989.

[34] T. Nobuoka, K. Kitamura, S. Iwahashi, T. Okino, Y. Liang, and S. Noda, "Two-dimensional beam-steering achieved using photonic-crystal lasers," in *CLEO: 2013 Technical Digest*, vol. 2, no. 1, 2013.

[35] E. Chow, S. Y. Lin, S. G. Johnson, P. R. Villeneuve, J. D. Joannopoulos, J. R. Wendt, G. A. Vawter, W. Zubrzycki, H. Hou, and A. Alleman, "Three-dimensional control of light in a two-dimensional photonic crystal slab," *Nature Letters*, vol. 407, no. September, pp. 983–986, 2000.

[36] L. Chen, W. Zhou, Z. Qiang, and G. J. Brown, "Spectral selectivity of photonic crystal infrared photodetectors," in *Nanomaterial Synthesis and Integration for Sensors, Electronics, Photonics, and Electro-Optics*, N. K. Dhar, A. K. Dutta, and M. S. Islam, Eds., vol. 6370, Oct 2006. [Online]. Available: http://proceedings.spiedigitallibrary.org/proceeding.aspx?articleid=1332271 pp. 63 701I–63 701I–7.

[37] S. Kalchmair, H. Detz, G. D. Cole, A. M. Andrews, P. Klang, M. Nobile, R. Gansch, C. Ostermaier, W. Schrenk, and G. Strasser, "Photonic crystal slab quantum well infrared photodetector," *Applied Physics Letters*, vol. 98, 2011. [Online]. Available: http://scitation.aip.org/content/aip/journal/apl/98/1/10.1063/1.3537954

[38] J. C. Knight, "Photonic band gap guidance in optical fibers," *Science*, vol. 282, no. 1998, pp. 1476–1478, 1998.

[39] A. A. Zakhidov, "Carbon structures with three-dimensional periodicity at optical wavelengths," *Science*, vol. 282, no. 1998, pp. 897–901, 1998.

[40] S. Y. Lin, J. G. Fleming, D. L. Hetherington, B. K. Smith, W. Zubrzycki, S. R. Kurtz, and J. Bur, "A three-dimensional photonic crystal operating at infrared wavelengths," *Nature*, vol. 394, pp. 251–253, 1998.

[41] J. R. Oh, Y. K. Lee, H. K. Park, and Y. R. Do, "Effects of symmetry, shape, and structural parameters of two-dimensional SiN_x photonic crystal on the extracted light from Y_2O_3:Eu_3^+ film," *Journal of Applied Physics*, vol. 105, p. 043103, 2009.

[42] M. Davanco, M. T. Rakher, D. Schuh, A. Badolato, and K. Srinivasan, "A circular dielectric grating for vertical extraction of single quantum dot emission," *Applied Physics Letters*, vol. 99, p. 041102, 2011.

[43] E. Matioli and C. Weisbuch, "Impact of photonic crystals on LED light extraction efficiency: Approaches and limits to vertical structure designs," *Journal of Physics D: Applied Physics*, vol. 43, p. 354005, 2010.

[44] H. Kyong, J. Jang, J.-H. Choi, J. Choi, J. Kim, J. S. Lee, B. Lee, Y. H. Choe, K.-D. Lee, S. H. Kim, K. Lee, S.-K. Kim, and Y.-H. Lee, "Light extraction enhancement from nano-imprinted photonic crystal GaN-based blue light-emitting diodes," *Optics Express*, vol. 14, no. 19, pp. 8654–8660, 2006.

[45] D. L. Barton and A. J. Fischer, "Photonic crystals improve LED efficiency," *SPIE Newsroom*, 2006.

[46] H. Kitagawa, M. Fujita, T. Suto, T. Asano, and S. Noda, "Green GaInN photonic-crystal light-emitting diodes with small surface recombination effect," *Applied Physics Letters*, vol. 98, no. 2011, p. 181104, 2012.

[47] M. Boroditsky, T. F. Krauss, R. Coccioli, R. Vrijen, R. Bhat, and E. Yablonovitch, "Light extraction from optically pumped light-emitting diode by thin-slab photonic crystals," *Applied Physics Letters*, vol. 75, no. 8, pp. 1036–1038, 1999.

[48] S. S. Schad, M. Scherer, M. Seyboth, and V. Schwegler, "Extraction efficiency of GaN-based LEDs," *Physica Status Solidi (A)*, vol. 130, no. 1, pp. 127–130, 2001.

[49] D.-H. Kim, C.-O. Cho, Y.-G. Roh, H. Jeon, Y. S. Park, J. Cho, J. S. Im, C. Sone, Y. Park, W. J. Choi, and Q.-H. Park, "Enhanced light extraction from GaN-based light-emitting diodes with holographically generated two-dimensional photonic crystal patterns," *Applied Physics Letters*, vol. 87, no. 203508, 2005.

[50] A. David, T. Fujii, E. Matioli, R. Sharma, S. Nakamura, L. Charles, F. De, and B. Orsay, "Omnidirectional light extraction in GaN LEDs using an Archimedean tiling photonic crystal," in *Physics and Simulation of Optoelectronic Devices*, M. Osinski, F. Henneberger, and Y. Arakawa, Eds., vol. 6115. SPIE, 2006. [Online]. Available: http://proceedings.spiedigitallibrary.org/

[51] M. F. Schubert, S. Chhajed, J. K. Kim, E. F. Schubert, and J. Cho, "Polarization of light emission by 460nm GaInN/GaN light-emitting diodes grown on (0001) oriented sapphire substrates," *Applied Physics Letters*, vol. 91, p. 051117, 2007.

[52] A. David, H. Benisty, and C. Weisbuch, "Optimization of diffracting photonic-crystals for high extraction efficiency LEDs," *Journal of Display Technology*, vol. 3, no. 2, pp. 133–148, 2007.

[53] J. J. Wierer, A. David, and M. M. Megens, "III-nitride photonic-crystal light-emitting diodes with high extraction efficiency," *Nature Photonics*, vol. 3, pp. 163–169, 2009.

[54] A. Z. Khokhar, K. Parsons, G. Hubbard, I. M. Watson, F. Rahman, D. S. Macintyre, C. Xiong, D. Massoubre, Z. Gong, E. Gu, N. P. Johnson, R. M. D. L. Rue, M. D. Dawson, S. J. Abbott, M. D. B. Charlton, and M. Tillin, "Emission characteristics of photonic crystal light-emitting diodes," *Applied Optics*, vol. 50, no. 19, pp. 3233–3239, 2011.

[55] K. McGroddy, A. David, E. Matioli, M. Iza, S. Nakamura, S. Denbaars, J. S. Speck, C. Weisbuch, and E. L. Hu, "Directional emission control and increased light extraction in GaN photonic crystal light emitting diodes," *Applied Physics Letters*, vol. 93, p. 103502, 2008.

[56] C. Wiesmann, K. Bergenek, N. Linder, and U. T. Schwarz, "Photonic crystal LEDs designing light extraction," *Laser and Photonics Reviews*, vol. 3, pp. 262–286, 2009.

[57] J. T. Zhang, E. Hao, V. W. Jones, T. L. Smith, S. A. Lamansky, H. T. Le, D. Qiu, W. B. Kolb, J. M. Battiato, and D. B. Stegall, "OLED light extraction films having nanoparticles and periodic structures," Patent 2012/0 234 460, 2012.

[58] W. H. Koo, W. Youn, P. Zhu, X.-H. Li, N. Tansu, and F. So, "Light extraction of organic light emitting diodes by defective hexagonal-close-packed array," *Advanced Functional Materials*, vol. 22, no. 16, pp. 3454–3459, August 2012. [Online]. Available: http://doi.wiley.com/10.1002/adfm.201200876

[59] Y.-J. Lee, S.-H. Kim, J. Huh, G.-H. Kim, and Y.-H. Lee, "A high-extraction-efficiency nanopatterned organic light-emitting diode," *Applied Physics Letters*, vol. 82, no. 21, pp. 3779–3781, 2003.

[60] Y. Li, F. Li, J. Zhang, C. Wang, S. Zhu, and H. Yu, "Improved light extraction efficiency of white organic light-emitting devices by biomimetic antireflective surfaces," *Applied Physics Letters*, vol. 96, p. 153305, 2010.

[61] M. Fujita, T. Ueno, T. Asano, S. Noda, H. Ohhata, T. Tsuji, H. Nakada, and N. Shimoji, "Organic light-emitting diode with ITO = organic photonic crystal," *Electronics Letters*, vol. 39, no. 24, 2003.

[62] V. W. Jones, S. A. Lamansky, J. M. Nelson, and H. T. Le, "OLED light extraction films with multi-periodic zones of nanostructures," Patent 2013/0 051 032, 2013.

[63] C. S. Choi, D.-y. Kim, S.-M. Lee, M. S. Lim, K. C. Choi, H. Cho, T.-W. Koh, and S. Yoo, "Blur-free outcoupling enhancement in transparent organic light emitting diodes: A nanostructure extracting surface plasmon modes," *Advanced Optical Materials*, vol. 1, pp. 687–691, 2013.

[64] A. P. Alivisatos, "Perspectives on the physical chemistry of semiconductor nanocrystals," *J. Phys. Chem.*, vol. 100, no. 95, pp. 13 226–13 239, 1996.

[65] D. V. Talapin and J. Steckel, "Quantum dot light-emitting devices," *MRS Bulletin*, vol. 38, pp. 685–691, 2013.

[66] M. Nirmal and L. Brus, "Luminescence photophysics in semiconductor nanocrystals," *Accounts of Chemical Research*, vol. 32, no. 5, pp. 407–414, 1999.

[67] T.-H. Kim, S. Jun, K.-S. Cho, B. L. Choi, and E. Jang, "Bright and stable quantum dots and their applications in full-color displays," *MRS Bulletin*, vol. 38, pp. 712–720, 2013.

[68] O. Chen, H. Wei, A. Maurice, M. Bawendi, and P. Reiss, "Pure colors from core shell quantum dots," *MRS Bulletin*, vol. 38, pp. 696–702, 2013.

[69] H. Volkan, S. Nizamoglu, T. Erdem, E. Mutlugun, N. Gaponik, and A. Eychmüller, "Quantum dot integrated LEDs using photonic and excitonic color conversion," *Nano Today*, vol. 6, pp. 632–647, 2011. [Online]. Available: http://dx.doi.org/10.1016/j.nantod.2011.10.006

[70] Z. Luo, Y. Chen, and S.-T. Wu, "Wide color gamut LCD with a quantum dot backlight," *Optics Express*, vol. 21, no. 22, p. 26269, 2013. [Online]. Available: http://www.opticsinfobase.org/abstract.cfm?URI=oe-21-22-26269

[71] G. J. Supran, Y. Shirasaki, K. W. Song, J.-M. Caruge, P. T. Kazlas, S. Coe-Sullivan, T. L. Andrew, M. G. Bawendi, and V. Bulovi, "QLEDs for displays and solid-state lighting," *MRS Bulletin*, vol. 38, pp. 703–711, 2013.

[72] H. S. Jang, H. Yang, S. W. Kim, J. Y. Han, S.-G. Lee, and D. Y. Jeon, "White light-emitting diodes with excellent color rendering based on organically capped CdSe quantum dots and Sr_3SiO_5:Ce_3^+,Li^+ phosphors," *Advanced Materials*, vol. 20, no. 14, pp. 2696–2702, jul 2008. [Online]. Available: http://doi.wiley.com/10.1002/adma.200702846

[73] X. Wang, W. Li, and K. Sun, "Stable efficient CdSe/CdS/ZnS core/multi-shell nanophosphors fabricated through a phosphine-free route for white light-emitting-diodes with high color rendering properties," *Journal of Materials Chemistry*, vol. 21, p. 8558, 2011.

[74] P. O. Anikeeva, J. E. Halpert, M. G. Bawendi, and V. Bulovic, "Quantum dot light-emitting devices with electroluminescence tunable over the entire visible spectrum," *Nano Letters*, vol. 9, no. 7, pp. 2532–2536, 2009.

[75] D. Bozyigit, O. Yarema, and V. Wood, "Origins of low quantum efficiencies in quantum dot LEDs," *Advanced Functional Materials*, vol. 23, pp. 3024–3029, 2013.

[76] J. Kwak, W. K. Bae, D. Lee, I. Park, J. Lim, M. Park, H. Cho, H. Woo, D. Y. Yoon, K. Char, S. Lee, and C. Lee, "Bright and efficient full-color colloidal quantum dot light-emitting diodes using an inverted device structure," *Nano Letters*, vol. 12, pp. 2362–2366, 2012.

[77] C. Dang and A. Nurmikko, "Beyond quantum dot LEDs: Optical gain and laser action in red, green, and blue colors," *MRS Bulletin*, vol. 38, pp. 737–742, 2013.

[78] V. Moiseyenko and M. Dergachov, "Quantum optics phenomena in synthetic opal photonic crystals," in *Quantum Optics and Laser Experiments*, D. S. Lyagushyn, Ed. InTech, 2012.

[79] M. Barth, A. Gruber, and F. Cichos, "Spectral and angular redistribution of photoluminescence near a photonic stop band," *Physical Review B*, vol. 72, 2005.

[80] P. Lodahl, A. Floris Van Driel, I. S. Nikolaev, A. Irman, K. Overgaag, D. Vanmaekelbergh, and W. L. Vos, "Controlling the dynamics of spontaneous emission from quantum dots by photonic crystals." *Nature*, vol. 430, no. 7000, pp. 654–657, 2004.

[81] D. Englund, D. Fattal, E. Waks, G. Solomon, B. Zhang, T. Nakaoka, Y. Arakawa, Y. Yamamoto, and J. Vuckovic, "Controlling the spontaneous emission rate of single quantum dots in a two-dimensional photonic crystal," *Physical Review Letters*, vol. 95, p. 013904, 2005.

[82] N. Ganesh, P. C. Mathias, W. Zhang, and B. T. Cunningham, "Distance dependence of fluorescence enhancement from photonic crystal surfaces," *Journal of Applied Physics*, vol. 103, pp. 1–6, 2008.

[83] F. Yang and B. T. Cunningham, "Enhanced quantum dot optical down-conversion using asymmetric 2D photonic crystals," *Optics Express*, vol. 19, no. 5, pp. 3908–18, 2011. [Online]. Available: http://www.ncbi.nlm.nih.gov/pubmed/21369216

[84] M. C. M. Lee, D. Hah, E. K. Lau, H. Toshiyoshi, and M. Wu, "MEMS-actuated photonic crystal switches," *IEEE Photonics Technology Letters*, vol. 18, no. 2, pp. 358–360, 2006.

[85] J. W. Jeong, B. Park, H. Keum, S. Kim, J. A. Rogers, and O. Solgaard, "High-reflectivity, broadband monolithic silicon photonic crystal mirrors on two-axis MEMS scanner by transfer-printing," *Optics Express*, vol. 21, no. 11, pp. 13 800–13 809, 2013.

[86] O. Levy, B. Z. Steinberg, M. Nathan, and A. Boag, "Ultrasensitive displacement sensing using photonic crystal waveguides," *Applied Physics Letters*, vol. 86, no. 10, pp. 1–3, 2005.

[87] Z. Xu, L. Cao, C. Gu, Q. He, and G. Jin, "Micro displacement sensor based on line-defect resonant cavity in photonic crystal," *Optics Express*, vol. 14, no. 1, pp. 298–305, 2006.

[88] W. Zhou, D. M. Mackie, M. Taysing-Lara, G. Dang, P. G. Newman, and S. Svensson, "Novel reconfigurable semiconductor photonic crystal-MEMS device," *Solid-State Electronics*, vol. 50, no. 6, pp. 908–913, 2006.

[89] Y. Shimoda, M. Ozaki, and K. Yoshino, "Electric field tuning of a stop band in a reflection spectrum of synthetic opal infiltrated with nematic liquid crystal," *Applied Physics Letters*, vol. 79, no. 22, pp. 3627–3629, 2001.

[90] M. Haurylau, S. P. Anderson, K. L. Marshall, and P. M. Fauchet, "Electrical modulation of silicon-based two-dimensional photonic bandgap structures," *Applied Physics Letters*, vol. 88, no. 6, 2006.

[91] Y. Saado, M. Golosovsky, D. Davidov, and A. Frenkel, "Tunable photonic band gap in self-assembled clusters of floating magnetic particles," *Physical Review B*, vol. 66, no. 19, pp. 1–7, 2002.

[92] H. Tian and J. Zi, "One-dimensional tunable photonic crystals by means of external magnetic fields," *Optics Communications*, vol. 252, no. 4-6, pp. 321–328, 2005.

[93] J. Zhou, C. Q. Sun, K. Pita, Y. L. Lam, Y. Zhou, S. L. Ng, C. H. Kam, L. T. Li, and Z. L. Gui, "Thermally tuning of the photonic band gap of SiO2 colloid-crystal infilled with ferroelectric BaTiO3," *Applied Physics Letters*, vol. 78, no. 5, pp. 661–663, 2001.

[94] K. Yoshino, Y. Shimoda, Y. Kawagishi, K. Nakayama, and M. Ozaki, "Temperature tuning of the stop band in transmission spectra of liquid-crystal infiltrated synthetic opal as tunable photonic crystal," *Applied Physics Letters*, vol. 75, no. 7, p. 932, 1999. [Online]. Available: http://scitation.aip.org/content/aip/journal/apl/75/7/10.1063/1.124558

[95] A. Faraon and J. Vučković, "Local temperature control of photonic crystal devices via micron-scale electrical heaters," *Applied Physics Letters*, vol. 95, no. 4, pp. 25–27, 2009.

[96] Y. Iwayama, J. Yamanaka, Y. Takiguchi, M. Takasaka, K. Ito, T. Shinohara, T. Sawada, and M. Yonese, "Optically tunable gelled photonic crystal covering almost the entire visible light wavelength region," *Langmuir: The ACS Journal of Surfaces and Colloids*, vol. 19, no. 4, pp. 977–980, 2003.

[97] Y. H. Cui, Q. Wu, W. Park, J. Jeon, M. J. Kim, and J. B. Lee, "MEMS-based mechanically tunable flexible photonic crystal," in *TRANSDUCERS 2009 - 15th International Conference on Solid-State Sensors, Actuators and Microsystems*. Denver, CO: IEEE, 2009, pp. 509–512.

[98] S. Kim and V. Gopalan, "Strain-tunable photonic band gap crystals," *Applied Physics Letters*, vol. 78, no. 20, pp. 3015–3017, 2001.

[99] V. Babin, P. Garstecki, and R. Holyst, "Photonic properties of an inverted face centered cubic opal under stretch and shear," *Applied Physics Letters*, vol. 82, no. 10, pp. 1553–1555, 2003.

[100] S. Jun and Y.-S. Cho, "Deformation-induced bandgap tuning of 2D silicon-based photonic crystals," *Optics Express*, vol. 11, no. 21, pp. 2769–2774, 2003.

[101] W. Park and J.-B. Lee, "Mechanically tunable photonic crystal structure," *Applied Physics Letters*, vol. 85, no. 21, p. 4845, 2004. [Online]. Available: http://scitation.aip.org/content/aip/journal/apl/85/21/10.1063/1.1823019

[102] O. Levy, B. Z. Steinberg, a. Boag, S. Krylov, and I. Goldfarb, "Mechanical tuning of two-dimensional photonic crystal cavity by micro electro mechanical flexures," *Sensors and Actuators, A: Physical*, vol. 139, no. 1-2 SPEC. ISS., pp. 47–52, 2007.

[103] M. Notomi, H. Taniyama, S. Mitsugi, and E. Kuramochi, "Optomechanical wavelength and energy conversion in high-Q double-layer cavities of photonic crystal slabs," *Physical Review Letters*, vol. 97, no. 2, pp. 2–5, 2006.

[104] W. Suh, M. F. Yanik, O. Solgaard, and S. Fan, "Displacement-sensitive photonic crystal structures based on guided resonance in photonic crystal slabs," *Applied Physics Letters*, vol. 82, no. 13, pp. 1999–2001, 2003.

[105] R. Perahia, J. D. Cohen, S. Meenehan, T. P. M. Alegre, and O. Painter, "Electrostatically tunable optomechanical "zipper" cavity laser," *Applied Physics Letters*, vol. 97, no. 19, pp. 1–3, 2010.

[106] I. W. Frank, P. B. Deotare, M. W. McCutcheon, and M. Loncar, "Programmable photonic crystal nanobeam cavities," *Optics Express*, vol. 18, no. 8, pp. 8705–8712, 2010.

[107] M. Winger, T. D. Blasius, T. P. Mayer Alegre, A. H. Safavi-Naeini, S. Meenehan, J. Cohen, S. Stobbe, and O. Painter, "A chip-scale integrated cavity-electro-optomechanics platform," *Optics Express*, vol. 19, no. 25, p. 24905, 2011.

[108] X. Chew, G. Zhou, F. S. Chau, J. Deng, X. Tang, and Y. C. Loke, "Dynamic tuning of an optical resonator through MEMS-driven coupled photonic crystal nanocavities," *Optics Letters*, vol. 35, no. 15, pp. 2517–2519, 2010.

[109] S. Sun, H. Kim, G. S. Solomon, and E. Waks, "Strain tuning of a quantum dot strongly coupled to a photonic crystal cavity," *Applied Physics Letters*, vol. 103, 2013.

[110] C. W. Wong, P. T. Rakich, S. G. Johnson, M. Qi, H. I. Smith, E. P. Ippen, C. Lionel, Y. Jeon, G. Barbastathis, and S.-G. Kim, "Strain-tunable silicon photonic band gap microcavities in optical waveguides," *Applied Physics Letters*, vol. 84, no. 8, p. 1242, 2004.

[111] E. Bormashenko, R. Pogreb, O. Stanevsky, Y. Biton, Y. Bormashenko, V. Streltsov, and Y. Socol, "2D photonic crystals deposited on polymer piezoelectric substrates - new kind of MOEMS," *Proceedings of the 2004 11th IEEE International Conference on Electronics, Circuits and Systems, 2004*, pp. 459–462, 2004.

[112] S. Benchabane, A. Khelif, J. Y. Rauch, L. Robert, and V. Laude, "Evidence for complete surface wave band gap in a piezoelectric phononic crystal," *Physical Review E - Statistical, Nonlinear, and Soft Matter Physics*, vol. 73, pp. 1–4, 2006.

[113] V. Laude, M. Wilm, S. Benchabane, and A. Khelif, "Full band gap for surface acoustic waves in a piezoelectric phononic crystal," *Physical Review E*, vol. 71, pp. 1–7, 2005.

[114] S. Kim and V. Gopalan, "Strain-tunable photonic band gap crystals," *Applied Physics Letters*, vol. 78, no. 20, pp. 3015–3017, 2001.

[115] S. Krishnamurthy and P. V. Santos, "Optical modulation in photonic band gap structures by surface acoustic waves," *Journal of Applied Physics*, vol. 96, no. 2004, pp. 1803–1810, 2004.

[116] R. Aigner, "MEMS in RF filter applications: Thin-film bulk acoustic wave technology," *Sensors Update*, vol. 12, pp. 175–210, 2003.

[117] N. Sinha, G. E. Wabiszewski, and S. M. Tanner, "Piezoelectric aluminum nitride nanoelectromechanical actuators," *Applied Physics Letters*, vol. 95, p. 053106, 2009.

[118] R. S. Weis and T. K. Gaylord, "Lithium niobate: summary of physical properties and crystal structure," *Applied Physics A*, vol. 37, pp. 191–203, 1985.

[119] J. G. Korvink and O. Paul, Eds., *MEMS: A practical guide to design, analysis, and applications.* Norwich, NY, USA: William Andrew Publishing, 2006.

[120] M.-A. Dubois, P. Muralt, and L. Sagalowicz, "Aluminum nitride thin films for microwave filter and microsystem applications," *MRS Proceedings*, vol. 604, no. 20, pp. 3032–3034, 1999.

[121] S. Gong and G. Piazza, "Design and analysis of lithium niobate-based high electromechanical coupling RF-MEMS resonators for wideband filtering," *IEEE Transactions on Microwave Theory and Techniques*, vol. 61, no. 1, pp. 403–414, 2013.

[122] Goodfellow, "Polyvinylidenefluoride Material Properties," 2015. [Online]. Available: http://www.goodfellow.com/E/Polyvinylidenefluoride.html

[123] S. Mishin and Y. Oshmyansky, "Thin films deposition for BAW devices," in *RF Bulk Acoustic Wave Filters for Communications*. Norwood, MA: Artech House, 2009, ch. 7, pp. 173–259.

[124] R. Patni, M. Joshi, S. Mehra, and A. Mohan, "Design of piezoelectric aluminum nitride MEMS resonator," in *World Congress on Engineering and Computer Science*, vol. I, San Francisco, CA, USA, 2011.

[125] S. Datta, "Intro to Piezoelectric BAW Resonator Modeling," 2013. [Online]. Available: http://www.comsol.com/blogs/piezoelectric-baw-resonator-modeling/

[126] M. Buchmeier, "SAW Device Schematic," 2007. [Online]. Available: https://commons.wikimedia.org/wiki/File:SAW_device.png

[127] J. Iannacci, "Design," in *Practical Guide to RF-MEMS*. Wiley-VCH, 2013, ch. 3, pp. 57–83.

[128] Y. Ding and R. Magnusson, "Band gaps and leaky-wave effects in resonant photonic-crystal waveguides," *Optics Express*, vol. 15, no. 2, pp. 680–694, 2007.

[129] Y. Ding and R. Magnusson, "Resonant leaky-mode spectral-band engineering and device applications," *Optics Express*, vol. 12, no. 23, pp. 5661–5674, 2004.

[130] N. Ganesh and B. T. Cunningham, "Photonic-crystal near-ultraviolet reflectance filters fabricated by nanoreplica molding," *Applied Physics Letters*, vol. 88, no. 7, p. 071110, 2006. [Online]. Available: http://scitation.aip.org/content/aip/journal/apl/88/7/10.1063/1.2173718

[131] M. Rippa, R. Capasso, P. Mormile, S. De Nicola, M. Zanella, L. Manna, G. Nenna, and L. Petti, "Bragg extraction of light in 2D photonic Thue-Morse quasicrystals patterned in active CdSe/CdS nanorod-polymer nanocomposites," *Nanoscale*, vol. 5, pp. 331–336, 2013.

[132] A. K. Kodali, M. Schulmerich, J. Ip, G. Yen, B. T. Cunningham, and R. Bhargava, "Narrowband midinfrared reflectance filters using guided mode resonance," *Analytical Chemistry*, vol. 82, no. 13, pp. 5697–5706, 2010.

[133] J. Herrnsdorf, B. Guilhabert, J. J. D. Mckendry, Z. Gong, D. Massoubre, and S. Zhang, "Hybrid organic / GaN photonic crystal light-emitting diode," *Applied Physics Letters*, vol. 101, p. 141122, 2012.

[134] K.-S. Cho, E. K. Lee, W.-J. Joo, E. Jang, T.-H. Kim, S. J. Lee, S.-J. Kwon, J. Y. Han, B.-K. Kim, B. L. Choi, and J. M. Kim, "High-performance crosslinked colloidal quantum-dot light-emitting diodes," *Nature Photonics*, vol. 3, no. June, pp. 341–345, 2009.

[135] D. J. Norris, "Electronic stucture in semiconductor nanocrystals: Optical experiment," in *Nanocrystal Quantum Dots*, 2nd ed., Victor I. Klimov, Ed. CRC Press, 2010, ch. 2.

[136] S. Diana, I. Meinel, and R. Sharma, "Photonic crystal-assisted light extraction from a colloidal quantum dot/GaN hybrid structure," *Nano Letters*, vol. 6, no. 6, pp. 1116–1120, 2006.

[137] N. Ganesh, W. Zhang, P. C. Mathias, E. Chow, J. A. N. T. Soares, V. Malyarchuk, A. D. Smith, and B. T. Cunningham, "Enhanced fluorescence emission from quantum dots on a photonic crystal surface," *Nature Nanotechnology*, vol. 2, pp. 515–520, 2007.

[138] L. Petti, M. Rippa, J. Zhou, L. Manna, M. Zanella, and P. Mormile, "Novel hybrid organic / inorganic 2D quasiperiodic PC : from diffraction pattern to vertical light extraction," *Nanoscale Research Letters*, vol. 6, no. 1, p. 371, 2011. [Online]. Available: http://www.nanoscalereslett.com/content/6/1/371

[139] J. R. Devore, "Refractive indices of rutile and sphalerite," *Journal of the Optical Society of America*, vol. 41, no. 6, pp. 416–419, 1951.

[140] M. Suzuki, "Optical films for LCD backlights," in *The Society for Information Display Conference*, Los Angeles, 2011.

[141] H.-F. Xiang, S.-C. Yu, C.-M. Che, and P. T. Lai, "Efficient white and red light emission from GaN/tris-(8-hydroxyquinolato) aluminum/platinum(II) meso-tetrakis(pentafluorophenyl) porphyrin hybrid light-emitting diodes," *Applied Physics Letters*, vol. 83, no. 8, p. 1518, 2003. [Online]. Available: http://scitation.aip.org/content/aip/journal/apl/83/8/10.1063/1.1604192

[142] W. K. Bae, S. Brovelli, and V. I. Klimov, "Spectroscopic insights into the performance of quantum dot light-emitting diodes," *MRS Bulletin*, vol. 38, no. September, pp. 721–730, 2013. [Online]. Available: http://www.journals.cambridge.org/abstract_S0883769413001826

[143] M. R. Singh, C. Racknor, and D. Schindel, "Controlling the photoluminescence of acceptor and donor quantum dots embedded in a nonlinear photonic crystal," *Applied Physics Letters*, vol. 101, p. 051115, 2012.

[144] I. D. Block, N. Ganesh, M. Lu, B. T. Cunningham, and S. Member, "A sensitivity model for predicting photonic crystal biosensor performance," *IEEE Sensors Journal*, vol. 8, no. 3, pp. 274–280, 2008.

[145] J. Rosenberg, R. V. Shenoi, S. Krishna, and O. Painter, "Design of plasmonic photonic crystal resonant cavities for polarization sensitive infrared photodetectors," *Optics Express*, vol. 18, no. 4, pp. 3672–86, mar 2010. [Online]. Available: http://www.ncbi.nlm.nih.gov/pubmed/20389377

[146] S. S. Wang and R. Magnusson, "Theory and applications of guided-mode resonance filters," *Applied Optics*, vol. 32, no. 14, pp. 2606–2613, 1993.

[147] R. Oulton, B. D. Jones, S. Lam, A. R. A. Chalcraft, D. Szymanski, D. O'Brien, T. F. Krauss, D. Sanvitto, A. M. Fox, D. M. Whittaker, M. Hopkinson, and M. S. Skolnick, "Polarized quantum dot emission from photonic crystal nanocavities studied under moderesonant enhanced excitation," *Optics Express*, vol. 15, no. 25, pp. 17 221–17 230, 2007.

[148] G. Lozano, D. J. Louwers, S. R. K. Rodriguez, S. Murai, O. T. A. Jansen, M. A. Verschuuren, and J. G. Rivas, "Plasmonics for solid-state lighting: enhanced excitation and directional emission of highly efficient light sources," *Light: Science & Applications*, vol. 2, 2013.

[149] S. R. K. Rodriguez, G. Lozano, M. A. Verschuuren, R. Gomes, K. Lambert, B. De Geyter, A. Hassinen, D. Van Thourhout, Z. Hens, and J. G. Rivas, "Quantum rod emission coupled to plasmonic lattice resonances: A collective directional source of polarized light," *Applied Physics Letters*, vol. 100, p. 111103, 2012.

[150] P.-H. Yao, C.-J. Chung, C.-L. Wu, and C.-H. Chen, "Polarized backlight with constrained angular divergence for enhancement of light extraction efficiency from wire grid polarizer," *Optics Express*, vol. 20, no. 5, pp. 4819–4829, 2012.

[151] H. Masui, N. N. Fellows, S. Nakamura, and S. P. DenBaars, "Optical polarization characteristics of light emission from sidewalls of primary-color light-emitting diodes," *Semiconductor Science and Technology*, vol. 23, p. 072001, 2008.

[152] E. Sutanto, Y. Tan, M. S. Onses, B. T. Cunningham, and A. G. Alleyne, "Electrohydrodynamic jet printing of micro-optical devices," *Manufacturing Letters*, vol. 2, no. 1, pp. 4–7, 2014. [Online]. Available: http://dx.doi.org/10.1016/j.mfglet.2013.10.007

[153] J.-U. Park, M. Hardy, S. J. Kang, K. Barton, K. Adair, D. K. Mukhopadhyay, C. Y. Lee, M. S. Strano, A. G. Alleyne, J. G. Georgiadis, P. M. Ferreira, and J. A. Rogers, "High-resolution electrohydrodynamic jet printing," *Nature Materials*, vol. 6, pp. 782–789, 2007.

[154] S. Mishra, K. L. Barton, A. G. Alleyne, P. M. Ferreira, and J. A. Rogers, "High-speed and drop-on-demand printing with a pulsed electrohydrodynamic jet," *Journal of Micromechanics and Microengineering*, vol. 20, no. 9, p. 095026, 2010.

[155] M. S. Onses, C. Song, L. Williamson, E. Sutanto, P. M. Ferreira, A. G. Alleyne, P. F. Nealey, H. Ahn, and J. A. Rogers, "Hierarchical patterns of three-dimensional block-copolymer films formed by electrohydrodynamic jet printing and self-assembly," *Nature Nanotechnology*, vol. 8, pp. 667–675, 2013.

[156] K. Shigeta, Y. He, E. Sutanto, S. Kang, A.-p. Le, R. G. Nuzzo, A. G. Alleyne, P. M. Ferreira, Y. Lu, and J. A. Rogers, "Functional protein microarrays by electrohydrodynamic jet printing," *Analytical Chemistry*, vol. 84, p. 1001210018, 2012.

[157] B. V. Wood, M. J. Panzer, J. Chen, M. S. Bradley, J. E. Halpert, M. G. Bawendi, and V. Bulovic, "Inkjet-printed quantum dot polymer composites for full-color AC-driven displays," *Advanced Materials*, vol. 21, pp. 1–5, 2009.

[158] A. Khan, K. Rahman, D. Soo, and K. Hyun, "Direct printing of copper conductive micro-tracks by multi-nozzle electrohydrodynamic inkjet printing process," *Journal of Materials Processing Technology*, vol. 212, pp. 700–706, 2012. [Online]. Available: http://dx.doi.org/10.1016/j.jmatprotec.2011.10.024

[159] E. Sutanto, K. Shigeta, Y. K. Kim, P. G. Graf, D. J. Hoelzle, K. L. Barton, A. G. Alleyne, P. M. Ferreira, and J. A. Rogers, "A multimaterial electrohydrodynamic jet (E-jet) printing system," *Journal of Micromechanics and Microengineering*, vol. 22, p. 045008, 2012.

[160] K. Barton, S. Mishra, K. A. Shorter, A. Alleyne, P. Ferreira, and J. Rogers, "A desktop electrohydrodynamic jet printing system," *Mechatronics*, vol. 20, no. 5, pp. 611–616, 2010. [Online]. Available: http://dx.doi.org/10.1016/j.mechatronics.2010.05.004

[161] B. H. Kim, M. S. Onses, J. B. Lim, S. Nam, N. Oh, H. Kim, K. J. Yu, J. W. Lee, J.-H. Kim, S.-K. Kang, C. H. Lee, J. Lee, J. H. Shin, N. H. Kim, C. Leal, M. Shim, and J. a. Rogers, "High-resolution patterns of quantom dots formed by electrohydrodynamic jet printing for light-emitting diodes," *Nano Letters*, vol. 15, no. 2, pp. 969–973, 2015. [Online]. Available: http://pubs.acs.org/doi/abs/10.1021/nl503779e

[162] I. D. Block, L. L. Chan, and B. T. Cunningham, "Large-area submicron replica molding of porous low- k dielectric films and application to photonic crystal biosensor fabrication," *Microelectronic Engineering*, vol. 84, pp. 603–608, 2007.

[163] Y. R. Do, Y. C. Kim, Y.-W. Song, C.-O. Cho, H. Jeon, Y.-J. Lee, S.-H. Kim, and Y.-H. Lee, "Enhanced Light Extraction from Organic Light-Emitting Diodes with 2D SiO2/SiNx Photonic Crystals," *Advanced Materials*, vol. 15, no. 14, pp. 1214–1218, 2003.

[164] M. Kahl, T. Thomay, V. Kohnle, K. Beha, M. Hagner, A. Halm, J. Ziegler, T. Nann, Y. Fedutik, U. Woggon, M. Artemyev, A. Leitenstorfer, and R. Bratschitsch, "Colloidal quantum dots in all-dielectric high-Q pillar microcavities," *Nano Letters*, vol. 7, no. 9, pp. 2897–2900, 2007.

[165] W. A. Saunders, K. J. Vahala, H. A. Atwater, and R. C. Flagan, "Resonance-enhanced spontaneous emission from quantum dots," *Journal of Applied Physics*, vol. 72, no. 2, pp. 806–808, 1992.

[166] D. Goldberg and V. M. Menon, "Enhanced amplified spontaneous emission from colloidal quantum dots in all-dielectric monolithic microcavities," *Applied Physics Letters*, vol. 102, p. 081119, 2013.

[167] P. Dimitrakis, P. Normand, C. Bonafos, E. Papadomanolaki, and E. Iliopoulos, "GaN quantum-dots integrated in the gate dielectric of metal-oxide-semiconductor structures for charge-storage applications," *Applied Physics Letters*, vol. 102, p. 053117, 2013.

[168] S. Prucnal, M. Turek, K. Gao, S. Zhuo, K. Pyszniak, A. Drozdziel, J. Zuk, and W. Skorupa, "III-V quantum dots in dielectrics made by ion implantation and flash lamp annealing," in *Proceedings of the IX International Conference ION 2012*, vol. 123, no. 5, Kazimierz Dolny, Poland, 2013, pp. 935–938.

[169] X. Li, F. He, G. Liu, Y. Huang, C. Pan, and C. Guo, "Fabrication of Ge quantum dots doped TiO_2 films with high optical absorption properties via layer-by-layer ion-beam sputtering," *Materials Letters*, vol. 67, pp. 369–372, 2012. [Online]. Available: http://dx.doi.org/10.1016/j.matlet.2011.09.111

[170] H. Kurisu, J. Horie, K. Nagoya, S. Yamamoto, and M. Matsuura, "Enhancement of exciton and biexciton luminescence in CuCl QDs on dielectric multilayers," *International Journal of Modern Physics B*, vol. 15, no. 28, 29 & 30, pp. 3841–3844, 2001.

[171] Z. Zeng, E. Paspalakis, C. S. Garoufalis, and A. F. Terzis, "Optical susceptibilities in singly charged ZnO colloidal quantum dots embedded in different dielectric matrices," *Journal of Applied Physics*, vol. 113, p. 054303, 2013.

[172] X. Song, M. Wang, T. Xing, J. Deng, J. Ding, and Z. Yang, "Fabrication of micro / nano-composite porous TiO_2 electrodes for quantum dot-sensitized solar cells," *Journal of Power Sources*, vol. 253, pp. 17–26, 2014. [Online]. Available: http://dx.doi.org/10.1016/j.jpowsour.2013.12.033

[173] C. Liu, Y. Li, W. Li, J. Zhu, J. Li, Q. Chen, and Y. Yang, "CdS quantum dots sensitized platelike WO3 photoelectrodes with a TiO2 buffer-layer," *Materials Letters*, vol. 120, pp. 170–173, 2014. [Online]. Available: http://dx.doi.org/10.1016/j.matlet.2014.01.053

[174] S. P. Anchala and K. C. Mathur, "Linear and nonlinear intersubband optical properties of Si quantum dot embedded in oxide , nitride , and carbide matrix," *Journal of Applied Physics*, vol. 110, p. 114320, 2011.

[175] V. L. Colvin, M. C. Schlamp, and A. P. Alivisatos, "Light-emitting-diodes made from cadmium selenide nanocrystals and a semiconducting polymer," *Nature*, vol. 370, pp. 354–357, 1994.

[176] G. G. See, L. Xu, M. S. Naughton, T. Tang, Y. Bonita, J. Joo, P. Trefonas, K. Deshpande, P. J. A. Kenis, R. G. Nuzzo, and B. T. Cunningham, "Region specific enhancement of quantum dot emission using interleaved two-dimensional photonic crystals," *Applied Optics*, vol. 54, no. 9, pp. 2302–2308, 2015.

[177] N. A. Hamizi and M. R. Johan, "Optical properties of CdSe quantum dots via Non-TOP based route," *International Journal of Electrochemical Science*, vol. 7, no. 9, pp. 8458–8467, 2012.

[178] P. V. Braun and P. Wiltzius, "Electrochemically grown photonic crystals," *Nature*, vol. 402, pp. 603–604, 1999.

[179] I. V. Soboleva, E. Descrovi, C. Summonte, A. A. Fedyanin, and F. Giorgis, "Fluorescence emission enhanced by surface electromagnetic waves on one-dimensional photonic crystals," *Applied Physics Letters*, vol. 94, no. 23, p. 231122, 2009. [Online]. Available: http://scitation.aip.org/content/aip/journal/apl/94/23/10.1063/1.3148671

[180] Y. Kurosaka, S. Iwahashi, Y. Liang, K. Sakai, E. Miyai, W. Kunishi, D. Ohnishi, and S. Noda, "On-chip beam-steering photonic-crystal lasers," *Lasers and Electro-Optics (CLEO) and Quantum Electronics and Laser Science Conference (QELS), 2010 Conference on*, vol. 4, no. July, pp. 447–450, 2010. [Online]. Available: http://dx.doi.org/10.1038/nphoton.2010.118

[181] P. Kramper, M. Agio, C. M. Soukoulis, A. Birner, F. Müller, R. B. Wehrspohn, U. Gösele, and V. Sandoghdar, "Highly directional emission from photonic crystal waveguides of subwavelength width," *Physical Review Letters*, vol. 92, no. March, pp. 113 903–1, 2004.

[182] S. Noda, M. Yokoyama, M. Imada, A. Chutinan, and M. Mochizuki, "Polarization mode control of two-dimensional photonic crystal laser by unit cell structure design," *Science*, vol. 293, pp. 1123–1125, 2001.

[183] G. G. See, L. Xu, E. Sutanto, A. G. Alleyne, R. G. Nuzzo, and B. T. Cunningham, "Polarized quantum dot emission in electrohydrodynamic jet printed photonic crystals," *Applied Physics Letters*, vol. 107, p. 051101, 2015.